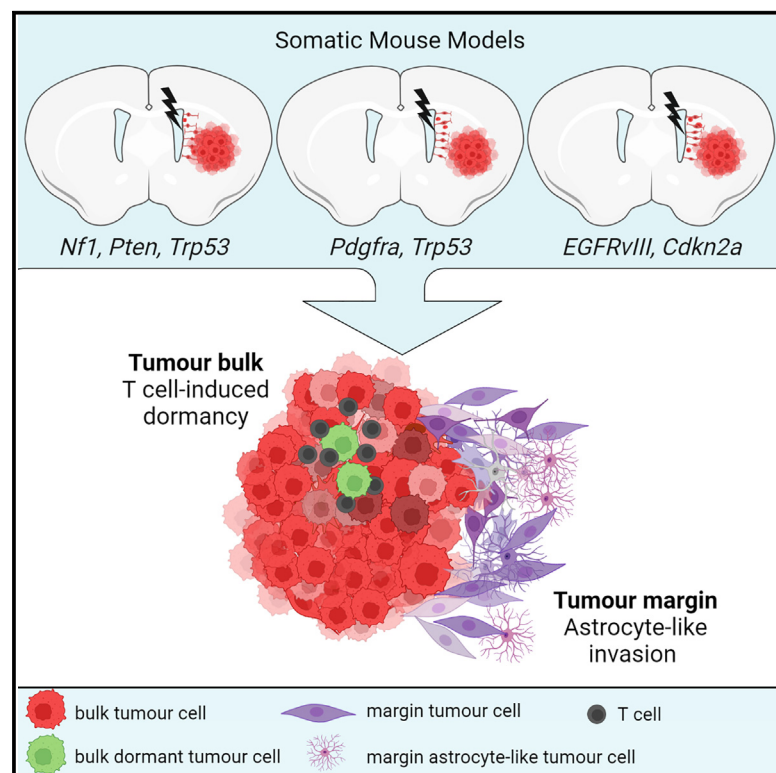


Glioblastoma cell fate is differentially regulated by the microenvironments of the tumor bulk and infiltrative margin

Graphical abstract



Authors

Claudia Garcia-Diaz, Anni Pöysti, Elisabetta Mereu, ..., Sergio A. Quezada, Holger Heyn, Simona Parrinello

Correspondence

s.parrinello@ucl.ac.uk

In brief

Garcia-Diaz et al. develop immunocompetent and disease-relevant somatic mouse models of glioblastoma to reveal that tumor bulk and margin cells have distinct biology, including differences in dormancy, differentiation trajectories, immune recruitment, and invasive and tumorigenic potential.

Highlights

- Somatic GBM mouse models were developed to compare tumor bulk and margin biology
- GBM cell fates are imposed by tumor region independent of driver mutations
- T cell-induced dormancy prevails in bulk, astrocyte-like differentiation in margin
- Bulk and margin cells are functionally distinct subpopulations



Article

Glioblastoma cell fate is differentially regulated by the microenvironments of the tumor bulk and infiltrative margin

Claudia Garcia-Diaz,^{1,11} Anni Pöysti,^{1,11} Elisabetta Mereu,^{2,3,11} Melanie P. Clements,^{1,12} Lucy J. Brooks,^{1,12} Felipe Galvez-Cancino,⁴ Simon P. Castillo,⁵ Wenhao Tang,⁶ Gordon Beattie,^{7,8} Lilas Courtot,¹ Sara Ruiz,² Federico Roncaroli,⁹ Yinyin Yuan,⁵ Samuel Marguerat,⁸ Sergio A. Quezada,⁴ Holger Heyn,^{2,10} and Simona Parrinello^{1,13,*}

¹Samantha Dickson Brain Cancer Unit, UCL Cancer Institute, London WC1E 6DD, UK

²CNAG-CRG, Centre for Genomic Regulation (CRG), Barcelona Institute of Science and Technology, 08028 Barcelona, Spain

³Josep Carreras Leukaemia Research Institute (IJC), Badalona, Barcelona, Catalonia, Spain

⁴Cancer Immunology Unit, Research Department of Haematology, UCL Cancer Institute, London WC1E 6DD, UK

⁵Division of Molecular Pathology & Centre for Evolution and Cancer, The Institute of Cancer Research, London SM2 5NG, UK

⁶Department of Mathematics, Imperial College London, London, UK

⁷CRUK City of London Centre Single Cell Genomics Facility, UCL Cancer Institute, University College London, London, UK

⁸Genomics Translational Technology Platform, UCL Cancer Institute, University College London, London, UK

⁹Geoffrey Jefferson Brain Research Centre, Division of Neuroscience, School of Biological Sciences, Faculty of Brain and Mental Health, University of Manchester, Manchester, UK

¹⁰Universitat Pompeu Fabra, Barcelona, Spain

¹¹These authors contributed equally

¹²These authors contributed equally

¹³Lead contact

*Correspondence: s.parrinello@ucl.ac.uk

<https://doi.org/10.1016/j.celrep.2023.112472>

SUMMARY

Glioblastoma (GBM) recurrence originates from invasive margin cells that escape surgical debulking, but to what extent these cells resemble their bulk counterparts remains unclear. Here, we generated three immuno-competent somatic GBM mouse models, driven by subtype-associated mutations, to compare matched bulk and margin cells. We find that, regardless of mutations, tumors converge on common sets of neural-like cellular states. However, bulk and margin have distinct biology. Injury-like programs associated with immune infiltration dominate in the bulk, leading to the generation of lowly proliferative injured neural progenitor-like cells (iNPCs). iNPCs account for a significant proportion of dormant GBM cells and are induced by interferon signaling within T cell niches. In contrast, developmental-like trajectories are favored within the immune-cold margin microenvironment resulting in differentiation toward invasive astrocyte-like cells. These findings suggest that the regional tumor microenvironment dominantly controls GBM cell fate and biological vulnerabilities identified in the bulk may not extend to the margin residuum.

INTRODUCTION

Glioblastoma (GBM) is the most common and aggressive primary brain tumor.^{1,2} Current standard of care, consisting of maximally safe surgical resection, chemo-, and radiotherapy, remains ineffective, leading to invariable recurrence and an average 5-year survival of 7%.¹

A main cause of therapy resistance is the diffuse infiltration of GBM cells into the normal brain.^{3,4} Infiltration precludes curative surgery, leading to tumor regrowth from cells that have invaded past the resection margin.^{3,4} Despite its crucial role in recurrence, however, the invasive GBM margin remains understudied, largely because of the paucity of available patient material, particularly the residual disease.⁴ Indeed, current knowledge of GBM biology originates largely from analysis of the tumor bulk

collected during biopsy or surgical de-bulking. Nonetheless, as invasive cells, rather than bulk cells, drive recurrence, potential differences between these populations would have profound therapeutic implications.

The pervasive molecular and cellular heterogeneity of GBM further limits the efficacy of both standard and targeted therapies.⁵ Molecular characterization of human GBM has revealed marked genetic, epigenetic, and transcriptional inter-tumoral heterogeneity.^{6–10} GBMs have been classified into three main molecular subtypes, termed proneural, classical, and mesenchymal, defined by distinct transcriptional signatures and associated driver mutations in platelet-derived growth factor receptor alpha (PDGFRA), epidermal growth factor receptor (EGFR), and nuclear factor 1 (NF1), respectively.^{6,11} Furthermore, GBMs display remarkable intra-tumor heterogeneity, with individual



tumors containing co-existing cell subpopulations of different genetics and subtypes.^{10,12–14}

At the cellular level, GBMs recapitulate developmental-like lineage hierarchies.^{12,14,15} The apex of this hierarchy is occupied by glioma stem-like cells (GSCs), capable of self-renewal and differentiation into non-stem tumor cells.^{15–18} Within the tumor bulk, lineage progression occurs toward neural-like fates, including oligodendrocyte progenitor cell (OPC-like), astrocyte- and neural progenitor-like states, or to a mesenchymal-like phenotype.^{12,14} These state transitions are modulated by driver mutations and by the immune microenvironment, with mutations biasing toward either OPC (PDGFR) or astrocyte-like fate (EGFR) and NF1-dependent microglia/macrophage infiltration promoting mesenchymal-like fate.^{11,14,19} In contrast, less is known about the lineage progression of invasive cells. Yet, the microenvironments of the bulk and margin are dramatically different, with bulk comprising hypoxic, necrotic, and angiogenic regions and margin containing largely normal brain tissue,²⁰ suggestive of distinct fate-choice pressures between the two regions. Consistently, molecular features and stemness differences have been reported between tumor cells isolated from bulk and proximal margin regions of patient GBM or patient-derived xenograft models.^{21–29} However, findings have been varied and at times conflicting, possibly because of heterogeneity in brain and tumor regions, highlighting the need for more standardized analysis.

Here, we compared the biology of bulk and margin GBM cells and the impact of tumor genetics. To do so, we developed three immunocompetent somatic mouse models of GBM driven by the main subtype-associated patient mutations. We found that, regardless of mutations, all three models converged on a finite set of cellular states that resemble normal and injured neural cell types. However, the frequency of these states was dominantly modulated by tumor region, resulting in the generation of biologically and functionally distinct tumor cell subpopulations. Our work suggests that bulk and margin microenvironments are major determinants of GBM biology.

RESULTS

Development of somatic GBM mouse models

To compare bulk and invasive tumor cells and understand the impact of genetic alterations on their biology, we developed three immunocompetent somatic mouse models of GBM carrying combinations of mutations commonly associated with the main human subtypes.^{6,11} This enabled us to functionally link tumor phenotypes to disease-relevant genotypes and model human GBM heterogeneity through combined analysis of the three models. Furthermore, the introduction of a tdTomato fluorescent reporter in all tumor cells allowed us to comprehensively sample the margin and discriminate tumor cells from normal brain cells.

Subtype-associated mutations were introduced into endogenous neural stem cells (NSCs) of the subventricular zone (SVZ) neurogenic niche, a frequent cell of origin in GBM patients.^{30,31} Specifically, the following mutations were used: EGFRvIII overexpression and *Cdkn2a* knockout (hereon EGFR model); *Pdgfra* overexpression (to mimic PDGFRA amplification and

elevated signaling associated with proneural tumors) and *Trp53* knockout (hereon *Pdgfr* model); *Nf1*, *Pten*, and *Trp53* knockout (hereon *Nf1* model). A non-integrating plasmid encoding for the PiggyBase transposase alone (*Pdgfr* and EGFR models) or with Cas9 (*Nf1* model) alongside an integrating piggyBac vector carrying the oncogenes, CRISPR guides to tumor suppressors, Cre recombinase and tdTomato, were co-electroporated into the lateral ventricles of *Trp53*^{fl/fl} (*Pdgfr* and *Nf1* models) or *Cdkn2a*^{fl/fl} (EGFR model) P2 pups (Figure 1A).³² Transient Cas9 expression inactivated the tumor suppressor genes, whereas PiggyBase-mediated integration of the piggyBac vector ensured stable oncogenes and tdTomato expression in targeted NSCs and their progeny. To ensure selective targeting of NSCs, Cas9 and Cre expression were driven by a truncated version of the human glial fibrillary acidic protein (GFAP) promoter (herein hGFAP_{MIN}).³³ Electroporation of a hGFAP_{MIN}-tdTomato reporter construct confirmed selective tomato expression in NSCs with radial glia morphology that were largely Ki67⁺/GFAP⁺ (Figures S1A–S1C). All genotypes generated tdTomato⁺ tumors with histological and molecular features of GBM, including vascular proliferation and necrosis, as well as expression of the GBM markers SOX2, OLIG2, and GFAP, within 8–15 weeks and with high penetrance (Figures 1B–1E). Crucially, the tumors displayed diffuse infiltration characteristic of human GBM (Figure 1B). Western blot analysis of primary tumor cells confirmed that the mutations were correctly introduced in each model (Figure S1D). Thus, the models recapitulate the human disease and can inform on GBM biology.

Tumor cell states differ between bulk and margin and are imposed by the microenvironment

We used single-cell RNA sequencing (scRNA-seq) to profile invasive tumor cells and their bulk counterparts in each model. The bulk and striatal margin regions (identified by fluorescence intensity, margin defined as region extending 1–2 mm from the bulk) of three tumors of each genotype were micro-dissected under fluorescence guidance, dissociated to single cells, and sorted using fluorescence-activated cell sorting (FACS) on tdTomato (Figures 2A and S2A).³⁴ The proportion of tdTomato⁺ tumor cells was lower at the margin relative to the bulk, confirming micro-dissection accuracy (Figure S2B). Transcriptomes from an average of 470 cells (range, 410–531 cells) per region were analyzed by SMART-seq2 (Figure 2A).³⁵

We first assessed the cellular composition of the tumors irrespective of region. Each model was analyzed independently and then all datasets were combined to identify common transcriptional patterns. Data integration, based on canonical correlation analysis, revealed that cells did not segregate by genotype but rather intermixed, converging onto eight main subpopulations or states across regions (Figure 2Bi, 2Bii and 2Biv). This is consistent with previous findings in human GBM^{12,14} and indicative of common and mutation-independent biological processes. Furthermore, all tumors contained mixtures of cells of all three transcriptional subtypes, four cellular states, and a GSC-like subpopulation with glial progenitor features identified in patients, further validating the models (Figures 2Biii, S2C, and S2D).^{11,12,14,38}

Harnessing the defined genetics and selective NSC targeting of the models, we next carried out a finer-grained analysis of

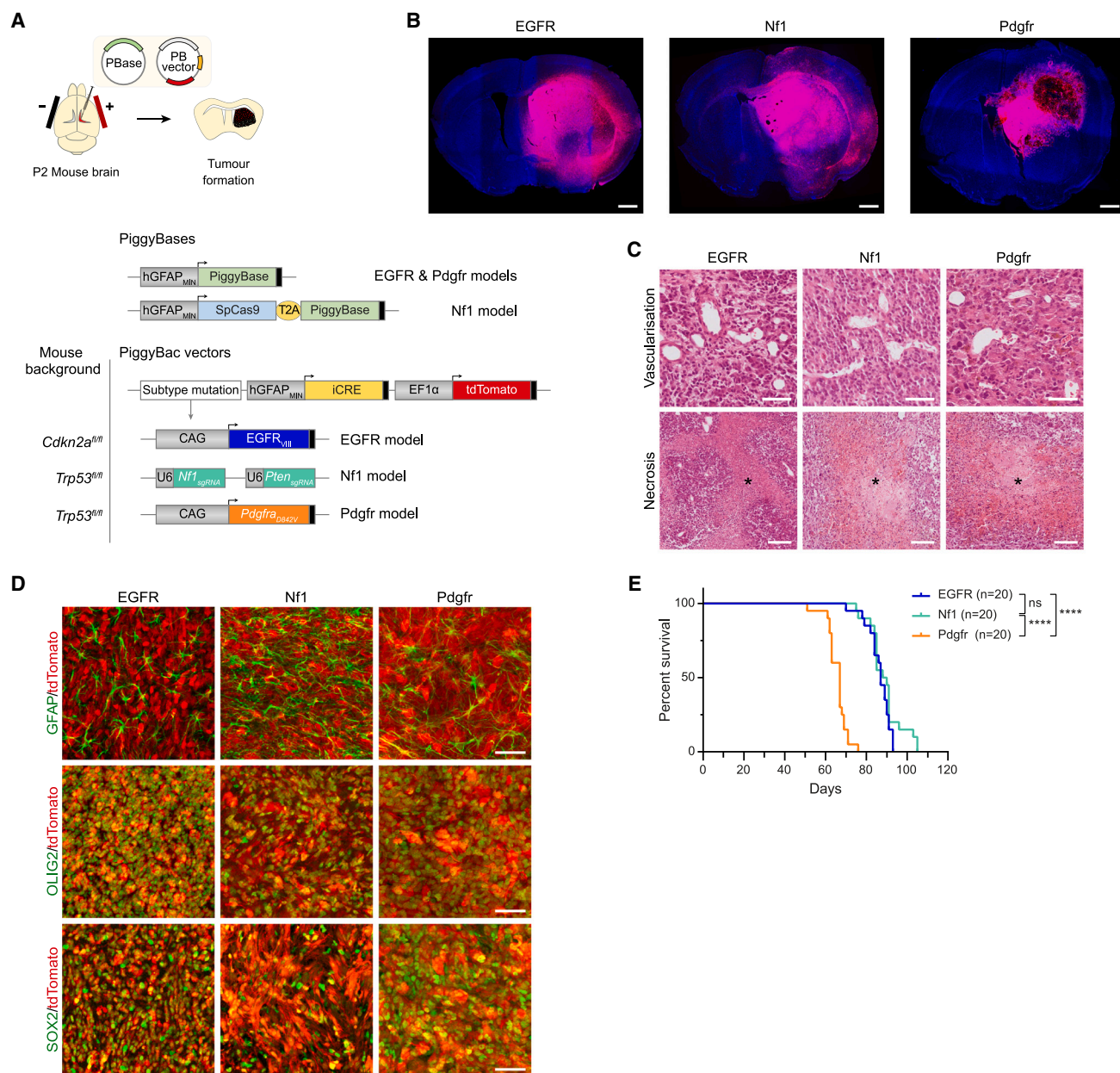
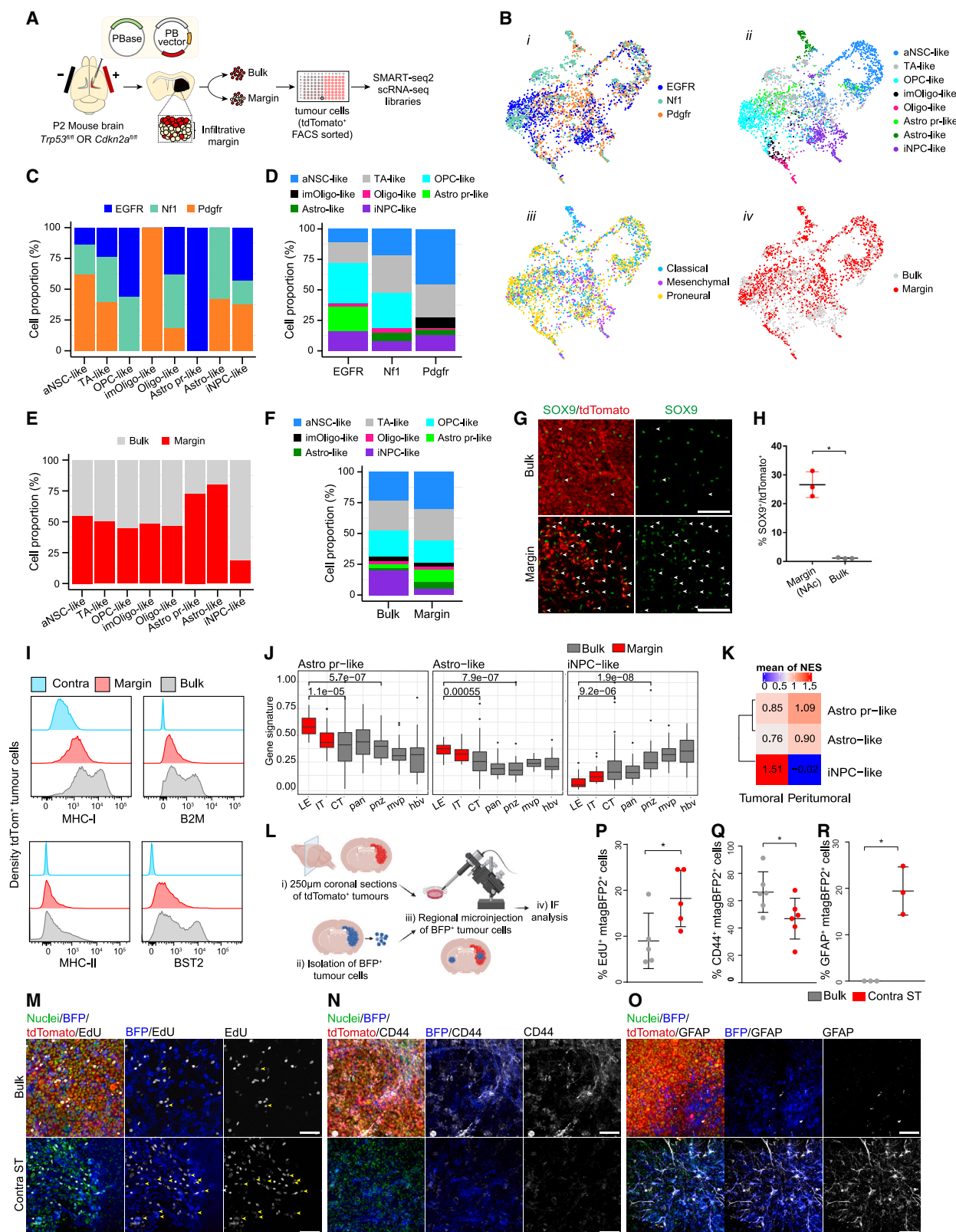


Figure 1. Development of somatic mouse models of GBM

(A) Schematic of method for tumor generation and piggyBac constructs. Black rectangle boxes denote polyA signal.
 (B) Representative fluorescence images of tumors of each genotype counterstained with DAPI (blue). Tumor cells are labeled by tdTomato (red). Scale bar, 1 mm.
 (C) Representative hematoxylin-eosin stainings of tumor models showing microvascular proliferation (top) and necrosis (asterisks, bottom). Scale bars, 50 μ m and 100 μ m, respectively.
 (D) Immunofluorescence staining for GFAP, OLIG2, and SOX2 (green) of tdTomato⁺ (red) EGFR, Nf1, and Pdgfr tumors, as indicated. Scale bar, 50 μ m.
 (E) Kaplan-Meier survival plots. n = 20. Log-rank Mantel Cox test. Median survival (days): EGFR = 87, Nf1 = 89, Pdgfr = 67. ****p < 0.0001. ns = not significant.
 See also Figure S1.

tumor cell fates and differentiation trajectories by comparing expression signatures of the eight clusters to normal SVZ neurogenesis. We used published scRNA-seq datasets of normal and ischemic SVZ because of the known links between injury and cancer (Figures S2E–S2H; Table S1).^{39–42} All tumors contained

cells with signatures of normal or injured neural progenitors (Figures 2Bii and S2E–S2H), four of which were shared among all genotypes. Specifically, all tumors contained cells similar to active NSCs (aNSC-like), transit amplifying progenitors/early neuroblasts (TA-like), oligodendrocytes (Oligo-like), and injured



(legend on next page)

NPCs that result from brain injury (iNPC-like). The aNSC-like cells were also highly enriched for human GSC signatures,^{12,38} thus corresponding to stem-like cells (Figure S2D). The iNPC-like state included mesenchymal-like cells described by Neftel et al.¹⁴ In addition, EGFR and Nf1 tumors contained cells with signatures similar to OPC-like cells and Pdgfr and Nf1 tumors contained cells with astrocyte-like subpopulations (Figures 2C and 2D). Interestingly, although Pdgfr tumors lacked OPC-like cells, they uniquely contained a subpopulation of cells with signatures of immature oligodendrocytes (imOligo-like), indicating that *Pdgfra* overexpression promotes maturation down the oligodendrocyte lineage while concomitantly preventing further differentiation, in line with its developmental roles (Figures 2C and 2D).^{34,43} Similarly, although EGFR tumors lacked more mature astrocyte-like cells, they contained a subpopulation with signatures of astrocyte progenitor-like cells (Astro pr-like), which was absent from other genotypes (Figures 2C and 2D). This suggests that EGFRvIII overexpression biases tumor cells toward astrogliogenesis, as reported for wild-type EGFR, while again blocking further differentiation.¹⁴ Thus, our models indicate that, regardless of genetics, tumor fates converge on a finite set of phenotypes that mimic neurogenesis, with driver mutations biasing toward specific cell fates, as observed in human GBM.¹⁴ They also reveal that mutations control the extent by which tumor cells differentiate, with sustained developmental RTK signaling blocking lineage progression.

We then examined the impact of tumor region on cellular states by comparing the frequency of the identified clusters in tumor bulk and margin (Figures 2Biv, 2E, and 2F). While all cell fates were detected in both regions, location influenced the frequency of specific states, with the bulk being enriched for iNPC-like cells and the margin for astrocyte-like fate. Interestingly, these biases were independent of genetics, as they were observed in all models, regardless of basal mutation-dependent lineage bias (Figure S2I). This suggests that tumor region is

dominant over driver mutations in modulating cell state and that margin and bulk biology may differ.

To determine whether transcriptional cell state changes corresponded to phenotypic changes, we examined astrocyte-like cells and iNPC-like cells in their spatial context using EGFR as a representative model. We used SOX9, a master regulator of astrogliogenesis highly expressed in the astrocyte-like clusters (Table S1), as a marker for Astro pr-like cells.⁴⁴ Immunofluorescence analysis confirmed that SOX9⁺ cells were rare within the bulk of the tumor (defined by nuclear density, see Figure S5B) and increased as cells invaded into the striatum (Figures 2G and 2H). However, SOX9 upregulation was heterogeneous within the margin, with a particularly strong enrichment in the nucleus accumbens (Figures 2G and 2H). Furthermore, SOX9⁺ Astro pr-like cells were present in both the proximal and distal margins, including the contralateral striatum, suggesting that this response was not linked to peri-tumoral astrogliosis⁴⁵ (Figure S2J). To test this more directly, we co-stained EGFR tumor sections for SOX9 together with the reactive astrocyte marker GFAP, which is not expressed in this model. We found no correlation between Astro-pr-like SOX9⁺ and areas of GFAP⁺ astrogliosis (Figure S2K), indicating that astrocyte-like differentiation is unlikely to be an inflammatory response.

To confirm the distribution of iNPC-like cells, we selected the major histocompatibility complex (MHC) class I markers H-2K^b and β_2 microglobulin (B2M), BST2, and MHC class II I-A/I-E as marker genes as they were all markedly increased in this cluster (Figure S2H; Table S1). The bulk and margin regions of 6 EGFR tumors were micro-dissected under fluorescence guidance, immunolabelled, and subjected to flow cytometry (FC) analysis. In agreement with the bioinformatics data, we found a much greater proportion of MHC-I^{high}, MHC class II^{high}, B2M^{high}, and BST2⁺ tdTomato⁺ iNPCs in the tumor bulk relative to the margin, confirming that iNPC-like fate occurs selectively in the bulk (Figures 2I and S1E).

Figure 2. Tumor cell states differ between bulk and margin

- (A) Schematic of experimental outline.
- (B) Uniform manifold approximation and projection (UMAP) visualization of 2,824 cells from the combined GBM tumor models. Cells are colored by (i) genotype, (ii) cell state, (iii) Verhaak molecular subtyping, and (iv) tumor region (bulk, margin).
- (C) Relative frequency of cell types across tumor genotypes.
- (D) Cell type composition per model.
- (E) Cell type composition of bulk and margin regions in the combined tumor models.
- (F) Relative proportions of cell types in the bulk and margin regions of the combined tumor dataset.
- (G) Representative immunofluorescence image of the bulk and margin regions of tdTomato⁺ (red) EGFR tumors stained for SOX9 (green). Scale bar, 100 μ m.
- (H) Quantifications of the number of SOX9⁺ astrocyte-like cells from (G). n = 3 EGFR tumors, >150 cells per tumor were counted. NAc, nucleus accumbens. Paired two-tailed Student's t test. Values are mean \pm SD. *p < 0.05.
- (I) FC analysis of indicated markers in tumor cells from bulk, margin, and contralateral (Contra) regions of EGFR tumors (n = 3).
- (J) Expression of indicated cell-type signatures in the bulk RNA-seq Ivy dataset (LE, leading edge; IT, infiltrating tumor; CT, cellular tumor; pan, pseudopalisading cells around necrosis; pnz, perinecrotic zone; mvp, microvascular proliferation; hbv, hyperplastic blood vessels).³⁶ Wilcoxon signed-rank test. Boxplots show 25th and 75th percentiles, median, and outliers.
- (K) Relative expression of indicated gene signatures in the scRNA-seq dataset from Yu et al.³⁷ Wilcoxon signed-rank test. The mean normalized enrichment score is shown.
- (L) Schematic of experimental outline.
- (M–O) Representative images of EdU (gray, M), CD44 (gray, N) and GFAP (gray, O) staining alongside tdTomato (red) and BFP (blue) fluorescence of organotypic slices. Scale bar, 100 μ m.
- (P–R) Quantification of immunofluorescence data shown in (M)–(O). (P) and (Q): n = 6, (R): n = 3, unpaired two-tailed Student's t test. Mean \pm SD. *p < 0.05.
- See also Figures S1 and S2 and Table S1.

We next assessed expression scores of the identified iNPC-, Astro pr-, and Astro-like signatures in spatially defined bulk RNA-seq (Ivy Glioblastoma Atlas Project³⁶) and scRNA-seq human GBM datasets.³⁷ This showed enrichment of Astro pr-like and Astro-like signatures at the tumor margin and iNPC signature within tumor bulk regions (Figures 2J and 2K), confirming the regional specificity of these phenotypes and their relevance to the human disease.

Together, these observations suggest that the tumor bulk and margin microenvironments might dominantly control tumor cell fate. To functionally test this hypothesis, we carried out re-injection experiments using an organotypic slice culture model. As SOX9 is strongly upregulated in cultured primary GSC and thus unsuitable as a marker of astrocyte-like fate in this system,⁴⁶ we used the Nf1 model that, unlike EGFR tumors, retains expression of more mature astrocyte markers, including GFAP (Table S1). Primary tumor cells were isolated from mtagBFP2-tagged Nf1 tumors and microinjected into the tumor bulk or contralateral striatum (to mimic the margin microenvironment) of organotypic brain slices prepared from tdTomato⁺ Nf1 tumor-bearing mice (Figure 2L). Within the bulk, mtagBFP2-Nf1 cells became less proliferative and increased expression of CD44, reminiscent of the iNPC-like phenotype, in the absence of GFAP expression (Figures 2M–2R). Conversely, cells injected in the contralateral striatum strongly upregulated GFAP expression, in line with induction of an astrocyte-like differentiation program, while remaining negative for iNPC markers and proliferating more actively (Figures 2M–2R). Thus, tumor phenotypes are biased by location and subject to significant cell-extrinsic control.

Bulk iNPC-like cells comprise a large proportion of dormant tumor cells

In the ischemic SVZ, iNPCs include primed quiescent cells poised for activation.³⁹ Consistent with this and observations in human tissue, the iNPC-like subpopulation was characterized by low proliferation in our models (Figure 3A), suggesting that it may represent dormant/quiescent tumor cells. To functionally test this idea, we modified the EGFR piggyBac construct to incorporate a Tet-ON inducible H2B-GFP reporter of label retention.⁴⁷ This approach allows *in vivo* detection of dormant tumor cells by pulse-chase experiments using doxycycline (Dox) administered in the drinking water. Following a chase period, proliferative cells dilute the label to varying extents while dormant cells retain levels of H2B-GFP protein comparable to non-chased controls. To simplify the piggyBac system and enable transformation of endogenous NSCs in any genetic background, we also introduced sgRNAs for *Cdkn2a* into the piggyBac backbone (Figure 3B), producing a fully integrated tool for tumor initiation. Like the EGFR piggyBac system, the EGFR-H2B-GFP construct produced tumors with histological features of GBM and with high penetrance (Figure S3A).

Dox was administered from electroporation until week 5 of tumor development followed by a 2- to 4-week chase period (Figure 3B). Immunofluorescence analysis before and after chase indicated that the H2B-GFP protein was incorporated in the chromatin of >90% of all tumor cells and effectively diluted over the chase period (Figures S3B and S3C). Furthermore, by

2 weeks of chase, H2B-GFP⁺ cells were largely negative for the proliferation marker Ki67, which was instead restricted to H2B-GFP[−] and a minority of H2B-GFP^{low} cells, confirming successful labeling of lowly proliferative/cell-cycle-arrested tumor cells (Figure S3D). To assess whether the cell-cycle arrest of H2B-GFP⁺ cells was reversible (a hallmark of dormancy⁴⁸), H2B-GFP⁺ cells (alongside tumor-matched H2B-GFP[−] cells as controls) were FACS sorted from EGFR tumors following a 2-week chase period and either cultured in GSC culture conditions or immediately orthotopically reinjected into syngeneic hosts. In both experiments, label-retaining H2B-GFP⁺ cells (LRCs) re-entered the cell cycle, as judged by their ability to proliferate *in vitro* and form secondary tumors *in vivo*, albeit more slowly than their H2B-GFP[−] counterparts (Figures S3E and S3F). Together, these data demonstrate that this system enables identification of dormant tumor cells, as previously reported using dye retention.^{49,50}

Having validated the approach, we next examined whether iNPC-like cells are LRCs by carrying out three complementary experiments. First, we examined the distribution of LRC H2B-GFP⁺ cells within the tumor *in situ* by immunofluorescence analysis. In agreement with the scRNA-seq findings (Figures 2E and 2F), the vast majority of LRCs were in the tumor bulk (Figure 3C), while rare or no LRCs were detected at the margin or contralaterally invaded regions (Figure S3G). Interestingly, we observed that, within the bulk, their distribution was not uniform but rather restricted to specific regions, with LRCs often found in clusters, suggestive of microenvironmental regulation (Figure 3C). Second, we carried out scRNA-seq of H2B-GFP⁺ LRCs and tumor-matched H2B-GFP[−] control cells acutely FACS sorted from EGFR tumors following a 2-week chase period and applied the iNPC and previously published quiescent signatures,^{51,52} alongside cell-cycle score (Figures 3D and S3I). This revealed a significant enrichment of all three signatures in LRCs with concomitant downregulation of cell-cycle-related genes. Finally, we measured expression levels of the iNPC markers CD44 and BST2 alongside Ki67 by FC and found a selective enrichment in H2B-GFP⁺ LRCs, which were also Ki67 low, as expected (Figures 3E, 3F, and S1E). We conclude that iNPC-like cells are LR tumor cells, induced to enter a dormancy-like state within the bulk of the tumor.

Dormant iNPC-like tumor cells are induced by interferon in T cell niches

To understand the signals that induce dormancy in the bulk, we examined the gene expression profile of iNPC-like cells. An analysis of top marker genes alongside gene ontology analysis showed an over-representation of immune genes and signatures, particularly interferon signaling, as reported in the ischemic SVZ (Figures 4A, 4B, and S4A; Table S2).³⁹ Furthermore, we found a parallel enrichment in interferon signaling and dormancy signatures in bulk tumor regions of the Ivy GBM dataset (Figure S4B).³⁶ This suggested that the iNPC-like state may be induced by interactions with immune cells via interferon signaling.

We, therefore, examined the distribution of the main immune compartments in our tumor models. All three models were infiltrated by immune cells as expected, with the EGFR model

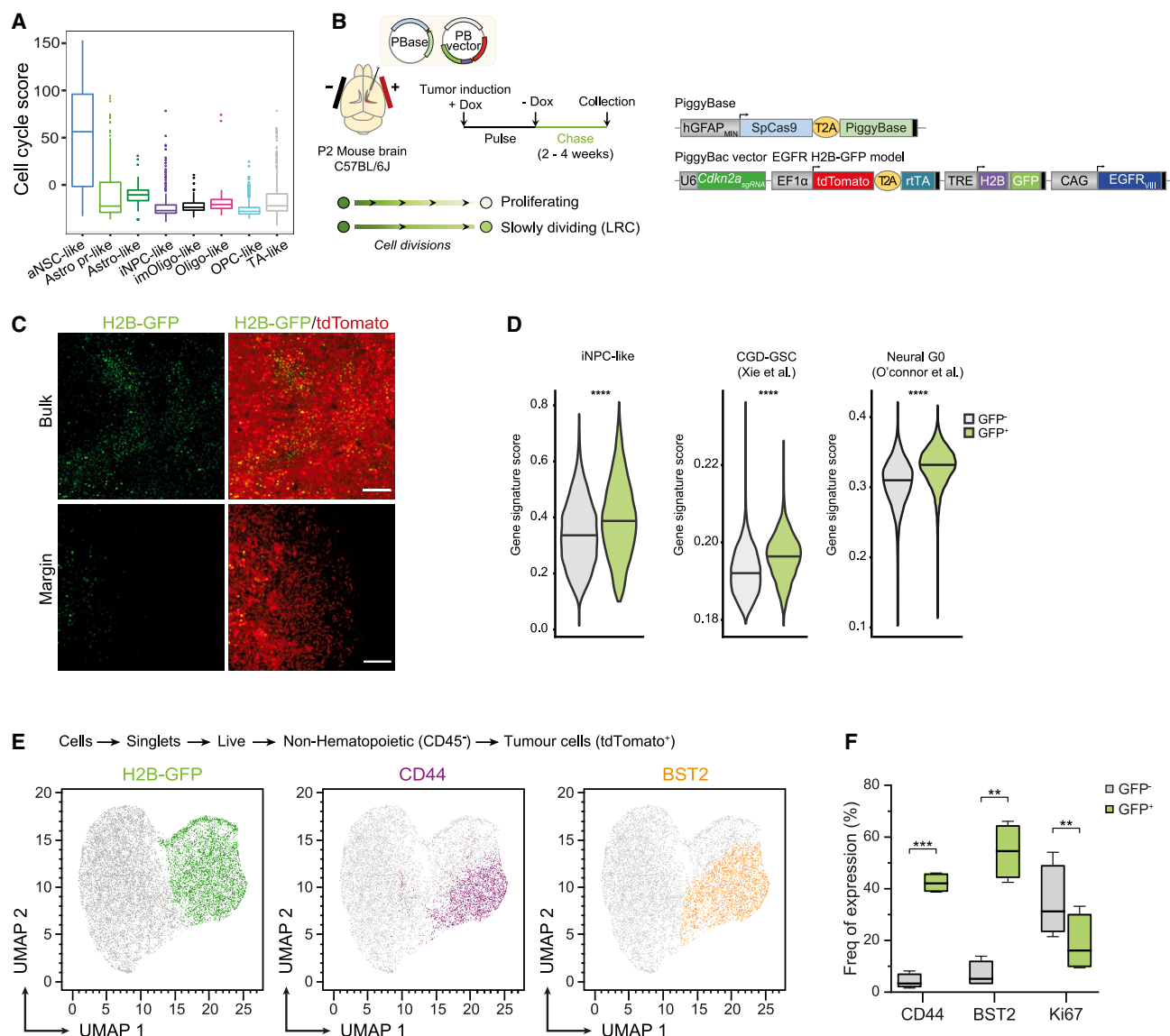
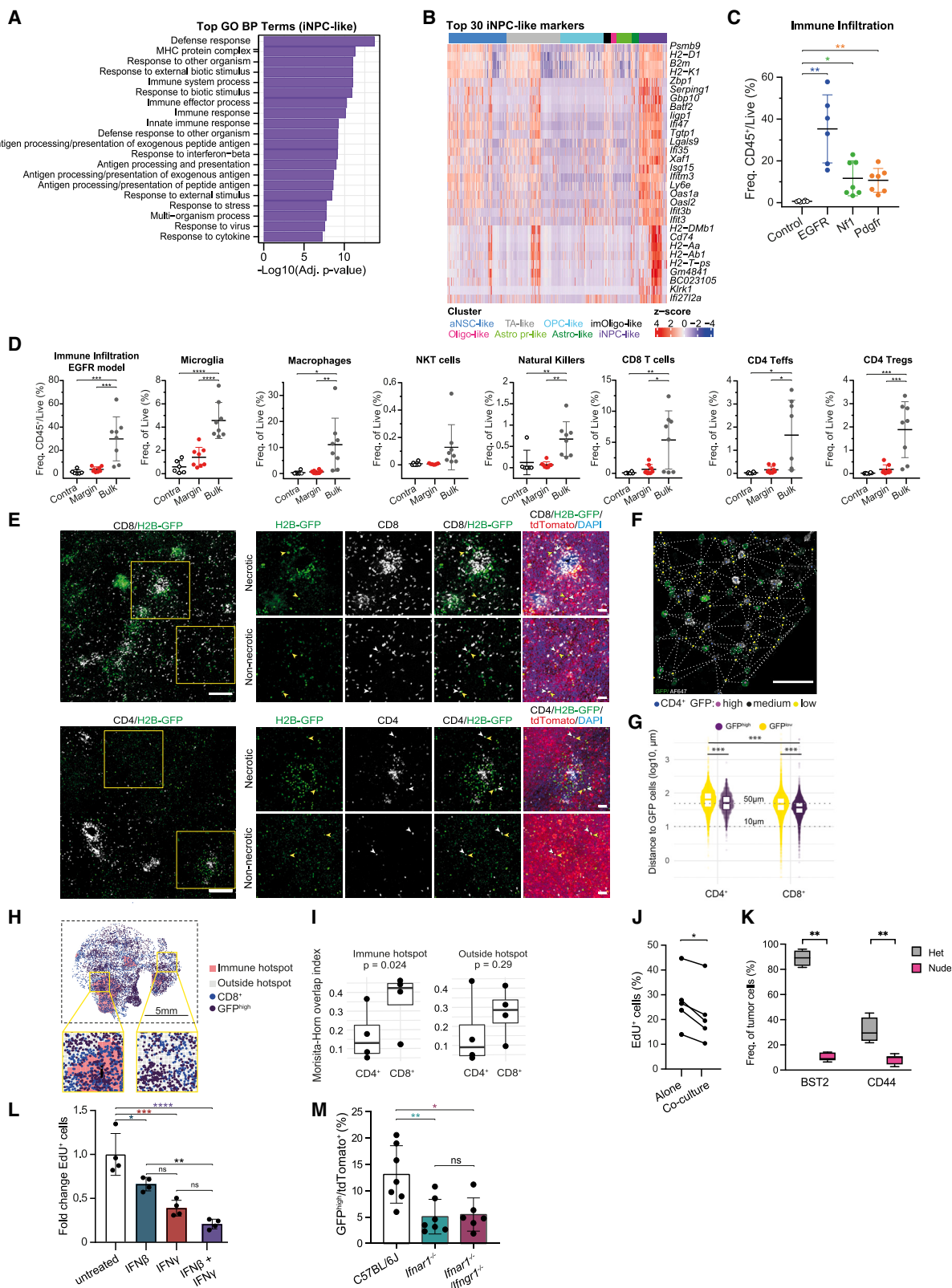


Figure 3. iNPC-like cells comprise a large proportion of dormant tumor cells

(A) Boxplots comparing cell-cycle signature score in each population across the three models. Boxplots show 25th and 75th percentiles, median, and outliers. (B) Schematic of experimental outline. (C) Representative fluorescence images of GFP (green) and tdTomato (red) in bulk and margin regions of EGFR-H2B-GFP tumors chased for 2 weeks. Scale bar, 100 μ m. (D) Relative expression of indicated gene signatures in the scRNA-seq dataset from acutely FACS-sorted GFP⁺ and GFP⁻ populations. Wilcoxon rank-sum test. Horizontal lines on violin plots indicate the median. ****p < 0.0001. (E) Uniform manifold approximation and projection (UMAP) projections of FC data for expression of GFP and iNPC-like cell markers CD44 and BST2 from bulk tumor regions (n = 4) at 2 weeks of chase. (F) Quantification of BST2-, CD44-, and Ki67-expressing H2B-GFP⁻ and H2B-GFP⁺ tumor cells from (E). Whisker plots show median and min-max value range. n = 4, two-tailed paired Student's t test. **p < 0.01, ***p < 0.001, ****p < 0.0001. See also [Figures S1](#) and [S3](#).

displaying the highest infiltration, possibly because of the expression of the EGFRvIII neoantigen ([Figures 4C](#) and [S1F](#)). Importantly, immune infiltration was not caused by tdTomato overexpression, as integration of a piggyBac construct encoding for tdTomato alone did not elicit an immune response

([Figures S4C](#) and [S4D](#)). We, therefore, assessed the immune microenvironment in bulk and margin by FC and immunofluorescence analysis, again using EGFR tumors as a model. The overall proportion of CD45 immune cells was significantly increased in the bulk, whereas the margin had levels of infiltration comparable



(legend on next page)

to tumor-free brain tissue (Figures 4D, S4E, and S1F). This indicates that the bulk accounts for the majority of the tumor immune infiltrate, whereas the margin may represent an immune-cold microenvironment. Differences in CD45 cells were reflected in all immune components analyzed, including microglia, macrophages, CD4 T cells, CD8 T cells, regulatory T cells, and natural killer cells, which were selectively enriched in the tumor bulk (Figures 4D, S4F–S4H, and S1F).

To test whether the increased immune infiltration of the bulk underpins dormancy, we first assessed the spatial distribution of immune cells relative to H2B-GFP⁺ LRCs by immunofluorescence. Although enriched in necrotic regions, microglia and macrophages were evenly distributed throughout the bulk (Figure S4G). Instead, rare natural killer cells were restricted to necrotic regions (Figure S4H). As the distribution of H2B-GFP⁺ cells was not uniform either within or outside necrotic patches, these patterns argue against a functional link between either cell type and LRCs (Figure 4E). In contrast, CD4 and CD8 T cells formed clusters in multiple tumor areas, including around necrotic regions, which seemed to co-localize at least partially with H2B-GFP⁺ LRC-rich regions (Figures 4E and S4F). Consistent with this, an analysis of the Neftel dataset¹⁴ confirmed that T cells are a main source of IFN- γ in human GBM (Figure S4I).

To quantify a potential spatial correlation between these populations, we used digital pathology. We applied supervised and semi-supervised algorithms to identify the exact location of T cells and H2B-GFP⁺ LRCs in immunofluorescence images of the tumors (balanced accuracy: LRCs = 0.96, T cells = 0.95). The LRC population was subdivided according to GFP intensity as a surrogate for their proliferative status, with H2B-GFP^{high} cells being the least and H2B-GFP^{low} the most proliferative (unsupervised three-class k means applied at each sample) and spatial relationships measured using cell-to-cell distance and

abundance-based approaches (Figure 4F). Both CD4 and CD8 T cells were found to be closer to H2B-GFP^{high} than H2B-GFP^{low} cells (Figure 4G) (generalized linear mixed model [GLMM], factor link type, T cell-GFP^{high} vs. T cell-GFP^{low}: $F = 193.467$, $p = 6.22e-44$), while CD8 T cells were closer to both H2B-GFP⁺ tumor populations than CD4 T cells (Figure 4G) (GLMM, factor T cell type CD8 vs. CD4: $F = 6.833$, $p = 0.039$), in the absence of a significant interaction between these variables (GLMM, interaction between factor T cell type and link type: $F = 0.045$, $p = 0.083$). Furthermore, measurement of the Morisita-Horn overlap index revealed that the co-localization of both CD8 and CD4 T cells with H2B-GFP^{high} was higher than 0 (CD8: $t(3) = 4.508$, $p = 0.02$; CD4: $t(3) = 2.4$, $p = 0.047$) within immune hotspots (defined by Getis-Ord's G^* on T cells distribution) and, controlling by the T cell/H2B-GFP⁺ ratio within immune hotspots, the co-localization of H2B-GFP^{high} cells with CD8 T cells was higher than with CD4 T cells (Figures 4H and 4I; $F(1,5) = 9.076$, $p = 0.029$; 95% confidence interval difference = 0.028–0.348). Outside of immune hotspots, only co-localization of H2B-GFP^{high} cells and CD8 T cells was significantly different from 0 (one-sided t test $t(3) = 4.048$, $p = 0.014$; CD4: $t(3) = 1.73$, $p = 0.09$), and no significant differences in co-localization with H2B-GFP^{high} cells were detected between CD4 and CD8 T cells (Figures 4H and 4I; GLM $F(1,5) = 1.39$, $p = 0.29$). However, H2B-GFP^{high} tumor cells showed overall higher co-localization with CD4 or CD8 T cells than with H2B-GFP^{low} cells resampled to control for difference in abundance between the two GFP subpopulations (Figure S4J). Together, this spatially resolved quantification suggests that H2B-GFP^{high} LRCs reside in close proximity to T cells, particularly, to the CD8 T cell compartment.

Next, we functionally assessed the role of T cells and interferon signaling in driving tumor dormancy in gain- and loss-of-function experiments. To examine T cells, primary EGFR tumor

Figure 4. Dormant tumor cells are induced by interferon in T cell niches

- (A) Gene Ontology (GO) enrichment analysis for iNPC-like cells. BP, biological process.
- (B) Heatmap of the top 30 iNPC-like markers. Columns are grouped by cell type (top bar). Normalized gene expressed values (Z scores) are shown.
- (C) FC analysis of CD45⁺ immune cells in the three tumor models and tumor-free contralateral hemispheres. Control: $n = 7$; EGFR: $n = 5$; Nf1: $n = 4$, and Pdgrf: $n = 4$. Two-tailed Mann-Whitney test. Mean \pm SD. * $p < 0.05$, ** $p < 0.01$.
- (D) FC analysis of indicated immune populations in the bulk and margin regions of EGFR tumors and contralateral brain (Contra). Contralateral: $n = 6$; bulk and margin: $n = 8$. One-way ANOVA with Tukey test. Mean \pm SD. * $p < 0.05$, ** $p < 0.01$, *** $p < 0.001$, **** $p < 0.0001$.
- (E) Representative immunofluorescence staining for CD8 (top) and CD4 (bottom) T cells in the bulk of EGFR-H2B-GFP tumors. Yellow boxes denote regions that are magnified on the right. Shown are examples of T cell-rich necrotic and non-necrotic regions surrounded by GFP⁺ LRCs. Direct cell-cell interactions between LRCs (yellow arrowheads) and T cells (white arrowheads) are indicated. Scale bar, 500 μ m (overview), 50 μ m (insets).
- (F) Example of cell detection, classification, and distance to neighboring cells after Delaunay triangulation (segmented white lines). Scale bar, 50 μ m.
- (G) Quantification of distances between H2B-GFP^{high} (GFP^{high}) or H2B-GFP^{low} (GFP^{low}) tumor cells and CD4 or CD8 T cells. Two-sided Student's t test with single-step p value adjustment. Boxplots show 25th and 75th percentiles, median, and outliers. *** $p < 0.001$.
- (H) Schematic representation of the distribution of CD8 T cells and H2B-GFP^{high} (GFP^{high}) cells in an EGFR-H2B-GFP tumor. Regions of T cell hotspots, detected by Getis-Ord's G^* , are shown in pink.
- (I) Morisita-Horn overlap indexes of indicated comparisons. >0 indicates a non-random distribution of cells. p value relates to comparison of H2B-GFP^{high} cells co-localization with CD4 or CD8 T cells. $n = 4$ tumors, one-sided Student's t test. Boxplots show 25th and 75th percentiles, median, and outliers.
- (J) FC analysis of the percentage of EdU⁺ tumor cells alone or co-cultured with activated T cells. $n = 5$ experiments across three independent cell lines. Wilcoxon one-tailed matched-pairs signed-rank test. * $p < 0.05$.
- (K) FC analysis of BST2⁺ and CD44⁺ iNPC-like tumor cells from orthotopic EGFR tumors developed in CD1^{nu/nu} mice (Nude, $n = 7$) or their littermate controls (Het, $n = 4$). Boxplots show the 25th and 75th percentiles, the median, and minimum and maximum values. Mann-Whitney test. ** $p < 0.01$.
- (L) FC analysis of the percentage of EdU⁺ cells in cultured primary EGFR tumor cells left untreated or treated with interferons. $n = 4$ experiments. One-way ANOVA with Tukey's multiple comparisons test. Mean \pm SD. * $p < 0.05$, *** $p < 0.001$, **** $p < 0.0001$.
- (M) FC analysis of H2B-GFP^{high} LRC in EGFR-H2B-GFP tumors generated in wild-type ($n = 7$), *lfnar1*^{-/-} ($n = 6$), or *lfnar1*^{-/-}; *lfnar1*^{-/-} ($n = 7$) animals. One-way ANOVA with Tukey's multiple comparisons test. Mean \pm SD. * $p < 0.05$, ** $p < 0.01$.
- See also Figures S1, S3, and S4 and Table S2.

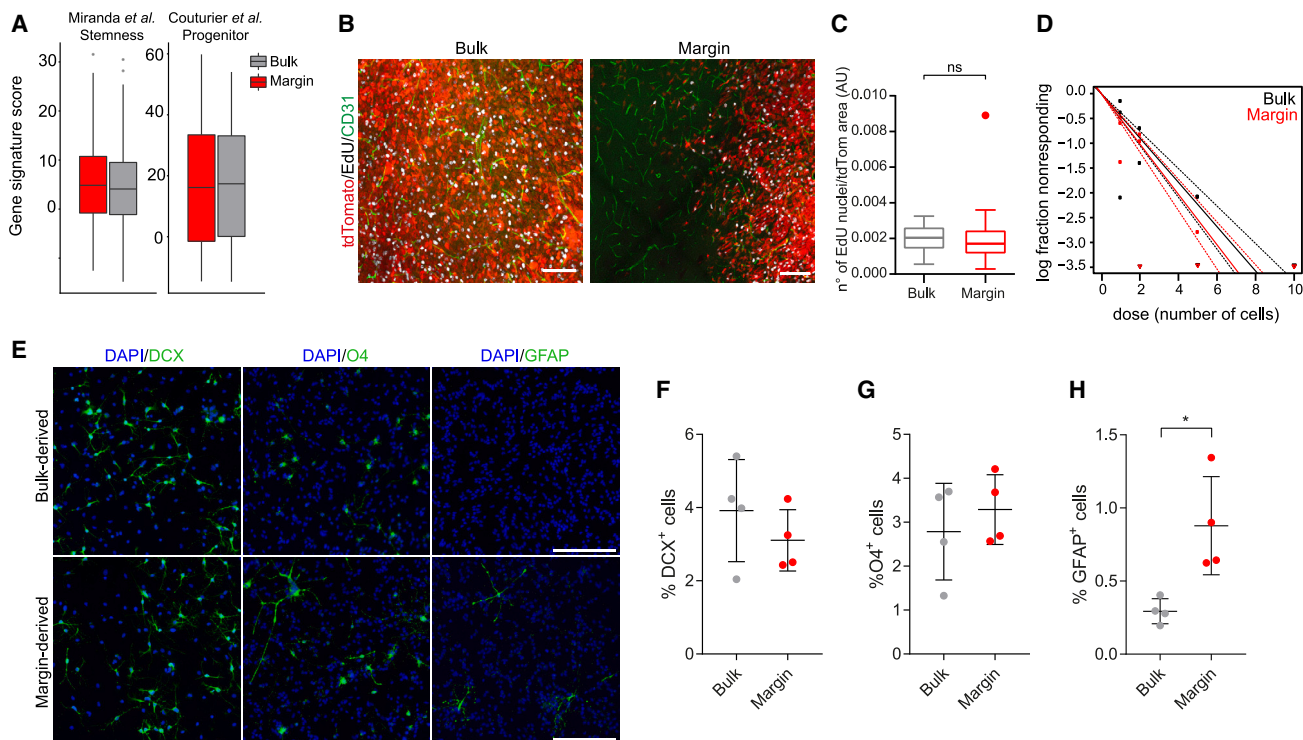


Figure 5. aNSC-like cells are not depleted at the margin but show a differentiation bias

(A) Analysis of indicated stemness gene signatures^{12,38} in bulk and margin aNSC-like cells in the combined models. Wilcoxon rank-sum test. Boxplots show 25th and 75th percentiles, median, and outliers.

(B and C) Representative immunofluorescence images and quantification of the number of EdU⁺ tumor cells in the bulk (gray) and margin (red) of EGFR tumors. Scale bar, 50 μ m. Six ROIs per tumor were counted, $n = 5$ tumors. Two-tailed Mann-Whitney test. Boxplots show 25th and 75th percentiles, median, and outliers. (D) Clonogenicity assay of primary bulk and margin GSC cultures. The slope of the line is the log-active cell fraction. The dotted lines give the 95% confidence interval. $n = 3$ experiments across three different cell lines.

(E–H) Representative immunofluorescence images (E) and associated quantifications (F–H) of bulk- or margin-derived primary differentiated tumor cells stained for DCX, O4, and GFAP (green) and counterstained with DAPI (blue). Scale bar, 100 μ m. Unpaired t test. Mean \pm SD. * $p < 0.05$.

See also Figure S5.

cells were co-cultured with freshly isolated T cells activated using antibodies to CD28, and proliferation was assessed by EdU incorporation. Exposure to T cells was sufficient to decrease the incorporation of tumor cells (Figure 4J). To explore whether T cells are also necessary for dormancy, we induced EGFR tumors in athymic CD1-nude mice, which lack T cells, or their heterozygous, immunocompetent littermate controls (Figure S4K) and examined proportions of INPCs by FC. To minimize confounding effects of the immunocompromised background on tumor development and progression, we used an orthotopic model for these experiments and analyzed tumors 2 weeks after implantation of primary EGFR tumor cells. We found a dramatic decrease in INPCs markers CD44 and BST2, consistent with dormancy being a T cell-driven phenotype (Figures 4K and S3J).

To examine interferon signaling, we first assessed effects of recombinant type I or II interferons alone or in combination on the proliferation of primary EGFR tumor cells and found a significant decrease in all treatment groups (Figure 4L). Furthermore, we induced EGFR-H2B-GFP tumors in *Ifnar1*^{−/−} or compound *Ifnar1*^{−/−}/*Ifngr1*^{−/−} mice, which are homozygous knockout for type I or type I/II interferon signaling, respectively, or in back-

ground-matched wild-type controls (Figure 4M).^{53,54} Following a 2-week chase period, we measured the proportion of H2B-GFP⁺ LRC in the three cohorts and found a significant decrease in both mutant strains relative to controls, indicative of a reduction in dormant cells in the absence of interferon signaling (Figure 4M). Importantly, interferon signaling-deficient and wild-type tumors had comparable levels of immune infiltration, indicating that the phenotype was not caused by a general decrease in immune activity in the mutants (Figure S4L). Thus, for at least a subset of tumor cells, dormancy is a bulk-specific phenotype induced by close interaction with T cells and depends on interferon signaling.

Margin GSCs are biased toward astrocyte-like differentiation

The enrichment of Astro- and Astro pr-like cells at the margin could result from an overall loss of stemness in this region and/or a bias toward astrocyte differentiation. To discriminate between these possibilities, we compared stemness signatures between bulk and margin aNSCs in the combined scRNA-seq data and found no changes (Figure 5A), consistent with their

similar frequencies in both regions (Figures 2E and 2F). We next examined their distribution within the tumor context by immunofluorescence analysis. As aNSC-like tumor cells contain the vast majority of cycling cells within the tumors (Figures 3A and S5A), we used proliferation as a proxy to label them selectively.⁵⁵ Mice were given a 2-h EdU pulse before sacrifice and the proportion of EdU⁺ aNSC-like cells quantified in bulk and margin regions of terminal tumors (Figures 5B, 5C, and S5B). Similar numbers of EdU⁺ cells were also detected within the perivascular space of both regions, one of the key GSC maintenance niches in GBM⁵⁶ (Figure S5C). Consistently, limiting dilution assays showed that primary GSC-enriched cultures derived from bulk and margin regions of EGFR tumors had similar clonogenic potential, a readout of self-renewal (Figure 5D).^{57,58}

To assess differentiation potential, tumor-derived bulk or margin GSC cultures were induced to differentiate by growth factor withdrawal and subjected to immunocytochemistry. While we observed no differences in the proportion of cells that differentiated toward oligodendrocyte-like (O4⁺) or neural progenitor-like (DCX⁺) states, margin-derived cells showed a significant bias toward astrocyte-like (GFAP⁺) differentiation (Figures 5E–5H). Thus, our data suggest that tumor region does not significantly impact the proportion of GSCs or their self-renewal but is an important determinant of fate choice.

Bulk and margin cells are functionally distinct subpopulations

Our results so far suggest that bulk and margin tumor cells may represent functionally distinct subpopulations. To test this hypothesis experimentally, early passage primary tumor cells isolated from bulk or margin regions of Pdgfr tumors were orthotopically re-injected into syngeneic mice. We used the Pdgfr model for this as it lacks astrocyte lineage bias, thereby minimizing confounding cell-intrinsic effects (Figure 2D). Both populations formed tumors at 100% penetrance, indicating that bulk and margin have comparable tumor-initiation potential (Figure 6A). However, pronounced differences in tumor development were observed. Bulk-derived tumors were hypercellular and circumscribed with a median survival of 49 days (Figures 6A–6C). In contrast, margin-derived tumors were significantly more infiltrative, failed to form a bona fide hypercellular bulk, and developed with much longer latency than bulk-derived tumors (median survival of 74 days) (Figures 6A–6C). Interestingly, these differences in invasive potential were at least in part cell intrinsic (or maintained *ex vivo*), as live imaging experiments revealed that early passage margin-derived tumor cells were significantly more motile than their tumor-matched bulk counterparts (Figure 6D), as previously reported for human GBM cells.²¹ However, treatment of margin-derived cells with IFN- γ to mimic the T cell-infiltrated and dormancy-inducing microenvironment of the bulk reversed their motility to the levels of bulk-derived cells. Together, these results suggest that the microenvironment imposes regional invasive phenotypes, which are then maintained within the tumor cells and their progeny.

To determine whether the molecular and cell fate differences between bulk and margin subpopulations are also maintained, we used immunofluorescence to examine iNPCs and Astro-like

cells alongside immune infiltration in the secondary tumors. Bulk-derived tumors displayed greater and more uniform expression of BST2 than margin-derived tumors (Figure 6G), which correlated with absence of EdU incorporation (Figure S6A), indicative of an enrichment of iNPCs. This was accompanied by robust immune infiltration of both Iba1⁺/CD68⁺ microglia/macrophages and CD3⁺ T cells, whereas both immune populations were much less frequent in margin-derived tumors (Figures 6E and 6F). Conversely, margin-derived tumor cells expressed high levels of SOX9 and GFAP across the entire lesion, whereas only occasional SOX9⁺ tumor cells were detected in bulk-derived tumors and most of them lacked GFAP expression (Figure 6H). However, we observed that, in bulk-derived lesions, tumor cells at the edge of the mass, which had begun to spread into the normal brain, dramatically upregulated SOX9 expression (Figure 6I). Thus, both bulk- and margin-derived tumors retain features of their region of origin, but bulk-derived cells reacquire properties of Astro-like cells upon exposure to the margin microenvironment.

Finally, we asked whether the distinct phenotypes of margin and bulk cells might impact their response to treatment. To address this, Pdgfra tumor-bearing mice were administered temozolomide, the standard of care chemotherapeutic agent in GBM, and cell death was quantified in both regions by cleaved caspase 3 (CC3) immunofluorescence. There was a significantly higher percentage of CC3⁺ tdTomato⁺ tumor cells within the bulk compared with the margin (Figure S6B), suggesting that margin cells may be more resistant to temozolomide. Consistent with this idea, analysis of the scRNA-seq data revealed that, similar to normal astrocytes,⁵⁹ Astro-like tumor cells selectively expressed high levels of several glutathione-s-transferases (Figure S6C). Glutathione-s-transferases play an important role in cellular detoxification and have been linked to therapy resistance, suggestive of a potential mechanism.⁶⁰ We, therefore, examined the correlation between glutathione-s-transferase gene expression and median survival in GBM patients from the CGGA and TCGA datasets and found a significant anti-correlation for the three glutathione-s-transferases most highly upregulated in Astro-like cells (Figure S6D). Together, our findings suggest that bulk and margin cells have distinct biology, with important implications for treatment.

DISCUSSION

The GBM margin is notoriously difficult to study in patients because of the challenges of sampling and identifying residual invasive tumor cells, particularly at distal sites.^{3,4} While robust mouse models of the disease have been developed, they often rely on cumbersome genetic breeding or lack reporters for conclusive identification of margin cells.⁶¹ To circumvent these problems, we developed three tractable somatic mouse models of GBM driven by common human subtype-associated mutations and carrying fluorescence and functional reporters. Overall, the models show striking similarities with the human disease, recapitulating the histology, transcriptional and cellular heterogeneity, cell states, and immune microenvironment of patient tumors.^{11,13,19} Consistent with recent patient studies, we found that, regardless of genetics, all tumors mirrored the main

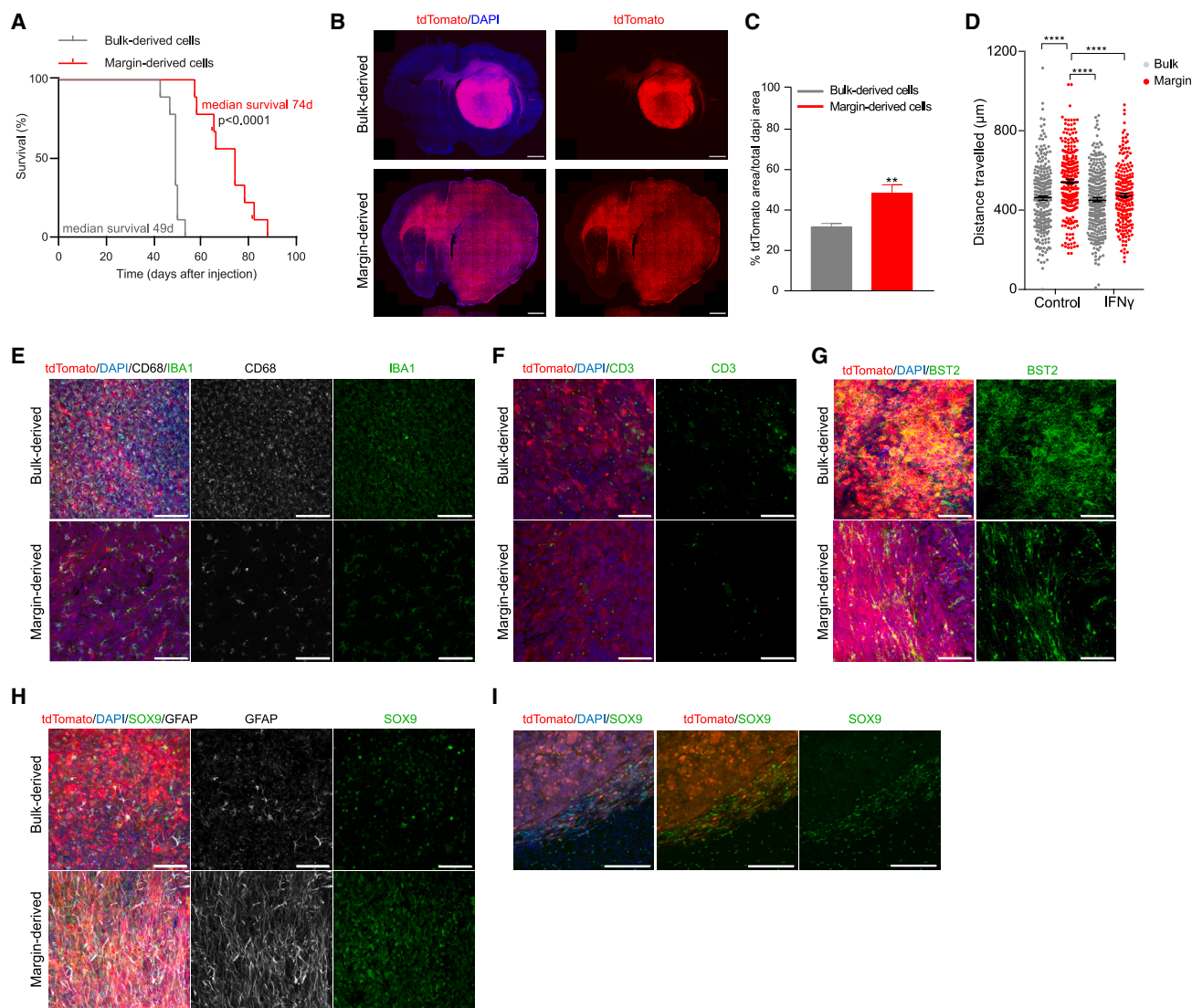


Figure 6. Bulk and margin phenotypes are maintained upon re-injection

(A) Kaplan-Meier survival plots for mice bearing secondary *Pdgfr* tumors derived from bulk and margin-derived cells. $n = 9$ per group. Log rank Mantel-Cox test. (B) Representative immunofluorescence images of bulk (top)- or margin (bottom)-derived tumors (tdTomato: red) and DAPI (blue) Scale bar, 1 mm. (C) Quantification of area infiltrated area (expressed as tdTomato⁺/DAPI). 3 sections were quantified for $n = 5$ animals per group. Two-tailed unpaired Student's *t* test. Mean \pm SEM. $^{**}p < 0.01$. (D) Total distance migrated by bulk- and margin-derived tumor cells in the presence or absence of IFN- γ (1,000 U/mL). Each dot represents a cell, $n = 272$ cells/group pooled from three independent experiments. $n = 3$ tumors. Two-way ANOVA. Mean \pm SEM. $^{****}p < 0.0001$. (E–H) Representative immunofluorescence images of bulk- or margin-derived tumors stained for markers of (E) iNPC-like cells (BST2; green), (F) microglial/macrophages (CD68; gray, IBA1; green), (G) T cells (CD3; green), and (H) Astro-like cells (GFAP; gray, SOX9; green). (I) Representative immunofluorescence image of SOX9 (green) expression at the margin of bulk-derived tumors. Scale bar, 100 μ m for (E–I). See also Figure S6.

developmental lineages of the brain, containing cells of astrocyte-like, oligodendrocyte-like, transit-amplifying progenitor/neuronal progenitor-like and GSC-like fate, alongside an injured/mesenchymal NPC-like states.^{12,14,62,63}

Although driver mutations biased the frequency of specific fates within our models, as was observed in human tumors,¹⁴ our results indicate that genetics plays an overall modest role

in driving tumor phenotypes. In contrast, we find that tumor region-specific microenvironmental signals are major determinants. Consistent with this, a recent spatially resolved analysis of primary bulk patient material reported that cell states are spatially segregated and influenced by inflammatory niches.⁶³ In our mouse models, the bulk regions of tumors of all genotypes were enriched for such injury-like states, which we show are

induced by interferons in T cell niches and lead to dormancy. This is reminiscent of the aged SVZ, where neural progenitors were shown to undergo quiescence in response to interferons released by infiltrating T cells.^{40,64} Furthermore, a link between the mesenchymal-like state and either interferon signaling or T cell signatures have previously been reported in patient GBM,^{19,63,65} again corroborating the relevance of our findings to the human disease. Interferons have also been previously linked to dormancy in a handful of other cancer types, which in a murine B cell lymphoma model was released by CD8 T cells.^{66–69}

At the margin, where the immune microenvironment resembled tumor-free brain, cells followed a developmental-like tumor hierarchy biased toward an astrocyte-like fate, even in Pdgfr tumors that display an intrinsic oligodendrocyte-like fate bias. Thus, although tumors are often compared with wounds that do not heal, our findings suggest that injury programs are mostly restricted to the tumor bulk and may not play a major role within the immune-cold margin, with implications for treatment, including checkpoint blockade immunotherapy.⁴² In line with our findings, a recent study proposed that human GSCs exist in either a neurodevelopmental or an inflammatory state.⁶² It would be important to explore whether there is a correlation between the GSC state and their location within the GBM bulk or margin in patients.

Our work suggests that GBM cells exhibit heterogeneous degrees of plasticity. Surprisingly, microenvironmentally imposed regional phenotypes were maintained upon re-injection. However, while bulk-derived tumors re-acquired astrocyte-like phenotypes upon invasion into the normal brain, margin phenotypes failed to re-form a tumor bulk or recruit immune cells in secondary hosts. This is consistent with recent analyses of paired primary and recurrent human GBM, which reported an enrichment for developmental-like signatures at recurrence.⁷⁰

In summary, our work reveals fundamental differences between the tumor bulk and margin and suggests that analysis of the bulk is not directly informative of margin biology or treatment. It further suggests that combinatorial therapies that take these differences into account will be required to improve patient outcome in this devastating disease.

Limitations of the study

The biological differences between bulk and margin tumor cells reported in this study were identified in models of primary treatment-naïve GBM. It would be important to determine the impact of standard of care treatment on these phenotypes. Our findings suggest that surgical resection, radiation, and chemotherapy, which are all potent injury signals, could contribute to resistance by inducing dormancy within the residual disease. It also remains to be determined if the astrocyte-like state is beneficial for invasion or contributes to the decreased immune infiltration of the margin, or indeed tumor regrowth following treatment. Finally, most of this work was carried out in mouse models. Although we found conservation with patient data at the transcriptomic level, future studies should continue to address the relevance of our mouse findings to the human disease. In this context, the use of 5-ALA fluorescence to FACS-purify tumor cells or postmortem resources such as the Posthumous Evaluation of

Advanced Cancer Environment (PEACE) study might offer exciting opportunities.²⁷

STAR★METHODS

Detailed methods are provided in the online version of this paper and include the following:

- KEY RESOURCES TABLE
- RESOURCE AVAILABILITY
 - Lead contact
 - Materials availability
 - Data and code availability
- EXPERIMENTAL MODEL AND STUDY PARTICIPANT DETAILS
- METHOD DETAILS
 - *In vivo* electroporation
 - Orthotopic injections
 - Tissue preparation and immunohistochemistry
 - Derivation and culture of cell lines
 - Regional injection of tumor-derived cells into organotypic tumor slices
 - T cell isolation from spleen and glioma-T cell co-culture
 - Interferon treatment and cell proliferation assay
 - Cell migration assay
 - Clonogenicity assay
 - Western blot
 - Plasmid generation
 - PiggyBases
 - PiggyBac plasmids
 - Flow cytometry analysis
 - Fluorescence-activated cell sorting for collection of single cells for RNA-sequencing
 - Single cell RNA library preparation (Smart-seq2)
 - Single cell RNA library preparation (10x)
 - Single cell RNA-seq data analysis (Smart-seq2)
 - Clustering
 - Data integration
 - Differential expression and GO analysis
 - Single-cell RNA-seq (10x) data pre-processing and analysis
 - Analysis of publicly available human datasets
 - Digital pathology
 - Spatial metrics for co-localization of T cells and H2B-GFP LRC
 - Assessment of colocalization between T cells and GFP subpopulations
- QUANTIFICATION AND STATISTICAL ANALYSIS

SUPPLEMENTAL INFORMATION

Supplemental information can be found online at <https://doi.org/10.1016/j.celrep.2023.112472>.

ACKNOWLEDGMENTS

This work was funded by Cancer Research UK (C55501/A21203, C55501/A22572, C25858/A28592), the Cancer Research UK City of London Centre Award (C7893/A26233), the Radiation Research Unit at the Cancer Research

UK City of London Centre Award (C7893/A28990), the NIHR Biomedical Research Centre (BRC507/CN/SP/101330), the Oli Hillsdon Foundation through The Brain Tumour Charity (GN-000595), the MCIN (PID2020-115439GB-I00), and the Fundació la Marató de TV3 (772/C/2019). We thank A. Berns for *Cdkn2a*^{-/-} mice, M. Aguet for *Ifnar1*^{-/-} and *Ifnar1*^{-/-};*Ifngr1*^{-/-} mice, P. Salomoni and S. Pollard for constructs, B. Antolin-Fontes for cloning, G. Rodriguez-Esteban for bioinformatics, M. Pathania for technical advice, A. Flanagan for histopathological advice, J. Manji for microscopy, and Y. Guo, G. Morrow, and B. Wilbourn for FACS. Graphical abstract and Figure 2L were created with [BioRender.com](https://www.biorender.com).

AUTHOR CONTRIBUTIONS

Conceptualization, S.P.; methodology, C.G.D., M.C., L.J.B., H.H., S.A.Q., Y.Y., and S.P.; software, E.M., H.H., S.P.C., and Y.Y.; validation, C.G.D., A.P., L.J.B., L.C., and M.C.; formal analysis, C.G.D., E.M., A.P., L.J.B., W.T., G.B., F.G.-C., S.P.C., L.C., and F.R.; investigation, C.G.D., M.C., A.P., L.J.B., F.G.-C., L.C., and S.R.; resources, H.H., S.A.Q., Y.Y., and S.P.; data curation, E.M., W.T., and G.B.; writing – original draft, C.G.D., M.C., E.M., and S.P.; writing – review & editing, L.J.B., A.P., M.C., S.M., and S.P.; visualization, C.G.D., E.M., A.P., S.P.C., G.B., and S.P.; supervision, H.H., S.A.Q., Y.Y., S.M., and S.P.; project administration, S.P.; funding acquisition, H.H., S.Q., Y.Y., and S.P.

DECLARATION OF INTERESTS

H.H. is a co-founder of and equity holder in Omniscope, a scientific advisory board member of MiRXES, and a consultant to Moderna.

INCLUSION AND DIVERSITY

We support inclusive, diverse, and equitable conduct of research.

Received: June 25, 2022

Revised: March 14, 2023

Accepted: April 19, 2023

Published: May 5, 2023

REFERENCES

- Miller, K.D., Ostrom, Q.T., Kruchko, C., Patil, N., Tihan, T., Cioffi, G., Fuchs, H.E., Waite, K.A., Jemal, A., Siegel, R.L., and Barnholtz-Sloan, J.S. (2021). Brain and other central nervous system tumor statistics, 2021. *CA. Cancer J. Clin.* 71, 381–406. <https://doi.org/10.3322/caac.21693>.
- McKinnon, C., Nandhabalan, M., Murray, S.A., and Plaha, P. (2021). Glioblastoma: clinical presentation, diagnosis, and management. *Brmj* 374, n1560. <https://doi.org/10.1136/bmj.n1560>.
- Cuddapah, V.A., Robel, S., Watkins, S., and Sontheimer, H. (2014). A neurocentric perspective on glioma invasion. *Nat. Rev. Neurosci.* 15, 455–465. <https://doi.org/10.1038/nrn3765>.
- Vehlow, A., and Cordes, N. (2013). Invasion as target for therapy of glioblastoma multiforme. *Biochim. Biophys. Acta* 1836, 236–244. <https://doi.org/10.1016/j.bbcan.2013.07.001>.
- Qazi, M.A., Vora, P., Venugopal, C., Sidhu, S.S., Moffat, J., Swanton, C., and Singh, S.K. (2017). Intratumoral heterogeneity: pathways to treatment resistance and relapse in human glioblastoma. *Ann. Oncol.* 28, 1448–1456. <https://doi.org/10.1093/annonc/mdx169>.
- Verhaak, R.G.W., Hoadley, K.A., Purdom, E., Wang, V., Qi, Y., Wilkerson, M.D., Miller, C.R., Ding, L., Golub, T., Mesirov, J.P., et al. (2010). Integrated genomic analysis identifies clinically relevant subtypes of glioblastoma characterized by abnormalities in PDGFRA, IDH1, EGFR, and NF1. *Cancer Cell* 17, 98–110. <https://doi.org/10.1016/j.ccr.2009.12.020>.
- Cancer Genome Atlas Research Network (2008). Comprehensive genomic characterization defines human glioblastoma genes and core pathways. *Nature* 455, 1061–1068. <https://doi.org/10.1038/nature07385>.
- Sturm, D., Witt, H., Hovestadt, V., Khuong-Quang, D.A., Jones, D.T.W., Konermann, C., Pfaff, E., Tönjes, M., Sill, M., Bender, S., et al. (2012). Hot-spot mutations in H3F3A and IDH1 define distinct epigenetic and biological subgroups of glioblastoma. *Cancer Cell* 22, 425–437. <https://doi.org/10.1016/j.ccr.2012.08.024>.
- Brennan, C.W., Verhaak, R.G.W., McKenna, A., Campos, B., Noshahr, H., Salama, S.R., Zheng, S., Chakravarty, D., Sanborn, J.Z., Berman, S.H., et al. (2013). The somatic genomic landscape of glioblastoma. *Cell* 155, 462–477. <https://doi.org/10.1016/j.cell.2013.09.034>.
- Sottoriva, A., Spiteri, I., Piccirillo, S.G.M., Touloumis, A., Collins, V.P., Marioni, J.C., Curtis, C., Watts, C., and Tavaré, S. (2013). Intratumor heterogeneity in human glioblastoma reflects cancer evolutionary dynamics. *Proc. Natl. Acad. Sci. USA* 110, 4009–4014. <https://doi.org/10.1073/pnas.1219747110>.
- Wang, Q., Hu, B., Hu, X., Kim, H., Squatrito, M., Scarpato, L., deCarvalho, A.C., Lyu, S., Li, P., Li, Y., et al. (2017). Tumor evolution of glioma-intrinsic gene expression subtypes associates with immunological changes in the microenvironment. *Cancer Cell* 32, 42–56.e6. <https://doi.org/10.1016/j.ccell.2017.06.003>.
- Couturier, C.P., Ayyadhury, S., Le, P.U., Nadaf, J., Monlong, J., Riva, G., Allache, R., Baig, S., Yan, X., Bourgey, M., et al. (2020). Single-cell RNA-seq reveals that glioblastoma recapitulates a normal neurodevelopmental hierarchy. *Nat. Commun.* 11, 3406. <https://doi.org/10.1038/s41467-020-17186-5>.
- Patel, A.P., Tirosh, I., Trombetta, J.J., Shalek, A.K., Gillespie, S.M., Wakiyama, H., Cahill, D.P., Nahed, B.V., Curry, W.T., Martuza, R.L., et al. (2014). Single-cell RNA-seq highlights intratumoral heterogeneity in primary glioblastoma. *Science* 344, 1396–1401. <https://doi.org/10.1126/science.1254257>.
- Neftel, C., Laffy, J., Filbin, M.G., Hara, T., Shore, M.E., Rahme, G.J., Richman, A.R., Silverbush, D., Shaw, M.L., Hebert, C.M., et al. (2019). An integrative model of cellular states, plasticity, and genetics for glioblastoma. *Cell* 178, 835–849.e21. <https://doi.org/10.1016/j.cell.2019.06.024>.
- Lan, X., Jörg, D.J., Cavalli, F.M.G., Richards, L.M., Nguyen, L.V., Vanner, R.J., Guilhamon, P., Lee, L., Kushida, M.M., Pellacani, D., et al. (2017). Fate mapping of human glioblastoma reveals an invariant stem cell hierarchy. *Nature* 549, 227–232. <https://doi.org/10.1038/nature23666>.
- Singh, S.K., Hawkins, C., Clarke, I.D., Squire, J.A., Bayani, J., Hide, T., Henkelman, R.M., Cusimano, M.D., and Dirks, P.B. (2004). Identification of human brain tumour initiating cells. *Nature* 432, 396–401. <https://doi.org/10.1038/nature03128>.
- Lathia, J.D., Mack, S.C., Mulkearns-Hubert, E.E., Valentim, C.L.L., and Rich, J.N. (2015). Cancer stem cells in glioblastoma. *Genes Dev.* 29, 1203–1217. <https://doi.org/10.1101/gad.261982.115>.
- Galli, R., Binda, E., Orfanelli, U., Cipelletti, B., Gritti, A., De Vitis, S., Fiocco, R., Foroni, C., Dimeco, F., and Vescovi, A. (2004). Isolation and characterization of tumorigenic, stem-like neural precursors from human glioblastoma. *Cancer Res.* 64, 7011–7021. <https://doi.org/10.1158/0008-5472.CAN-04-1364>.
- Hara, T., Chanoch-Myers, R., Mathewson, N.D., Myskiw, C., Atta, L., Bussemma, L., Eichhorn, S.W., Greenwald, A.C., Kinker, G.S., Rodman, C., et al. (2021). Interactions between cancer cells and immune cells drive transitions to mesenchymal-like states in glioblastoma. *Cancer Cell* 39, 779–792.e11. <https://doi.org/10.1016/j.ccell.2021.05.002>.
- Brooks, L.J., and Parrinello, S. (2017). Vascular regulation of glioma stem-like cells: a balancing act. *Curr. Opin. Neurobiol.* 47, 8–15. <https://doi.org/10.1016/j.conb.2017.06.008>.
- Glas, M., Rath, B.H., Simon, M., Reinartz, R., Schramme, A., Trageser, D., Eisenreich, R., Leinhaas, A., Keller, M., Schildhaus, H.U., et al. (2010). Residual tumor cells are unique cellular targets in glioblastoma. *Ann. Neurol.* 68, 264–269. <https://doi.org/10.1002/ana.22036>.

22. Hoelzinger, D.B., Mariani, L., Weis, J., Woyke, T., Berens, T.J., McDonough, W.S., Sloan, A., Coons, S.W., and Berens, M.E. (2005). Gene expression profile of glioblastoma multiforme invasive phenotype points to new therapeutic targets. *Neoplasia* 7, 7–16. <https://doi.org/10.1593/neo.04535>.
23. Bastola, S., Pavlyukov, M.S., Yamashita, D., Ghosh, S., Cho, H., Kagaya, N., Zhang, Z., Minata, M., Lee, Y., Sadahiro, H., et al. (2020). Glioma-initiating cells at tumor edge gain signals from tumor core cells to promote their malignancy. *Nat. Commun.* 11, 4660. <https://doi.org/10.1038/s41467-020-18189-y>.
24. Molina, J.R., Hayashi, Y., Stephens, C., and Georgescu, M.M. (2010). Invasive glioblastoma cells acquire stemness and increased Akt activation. *Neoplasia* 12, 453–463. <https://doi.org/10.1593/neo.10126>.
25. Piccirillo, S.G.M., Combi, R., Cajola, L., Patrizi, A., Redaelli, S., Bentivegna, A., Baronchelli, S., Maira, G., Pollo, B., Mangiola, A., et al. (2009). Distinct pools of cancer stem-like cells coexist within human glioblastomas and display different tumorigenicity and independent genomic evolution. *Oncogene* 28, 1807–1811. <https://doi.org/10.1038/ncr.2009.27>.
26. Siebzehnrubl, F.A., Silver, D.J., Tugertimur, B., Deleyrolle, L.P., Siebzehnrubl, D., Sarkisian, M.R., Devers, K.G., Yachnis, A.T., Kupper, M.D., Neal, D., et al. (2013). The ZEB1 pathway links glioblastoma initiation, invasion and chemoresistance. *EMBO Mol. Med.* 5, 1196–1212. <https://doi.org/10.1002/emmm.201302827>.
27. Smith, S.J., Diksin, M., Chhaya, S., Sairam, S., Estevez-Cebrero, M.A., and Rahman, R. (2017). The invasive region of glioblastoma defined by 5ALA guided surgery has an altered cancer stem cell marker profile compared to central tumour. *Int. J. Mol. Sci.* 18, 2452. <https://doi.org/10.3390/ijms18112452>.
28. Venkataramani, V., Yang, Y., Schubert, M.C., Reyhan, E., Tetzlaff, S.K., Wißmann, N., Botz, M., Soyka, S.J., Beretta, C.A., Pramatarov, R.L., et al. (2022). Glioblastoma hijacks neuronal mechanisms for brain invasion. *Cell* 185, 2899–2917.e31. <https://doi.org/10.1016/j.cell.2022.06.054>.
29. Darmanis, S., Sloan, S.A., Croote, D., Mignardi, M., Chernikova, S., Samghabadi, P., Zhang, Y., Neff, N., Kowarsky, M., Caneda, C., et al. (2017). Single-cell RNA-seq analysis of infiltrating neoplastic cells at the migrating front of human glioblastoma. *Cell Rep.* 21, 1399–1410. <https://doi.org/10.1016/j.celrep.2017.10.030>.
30. Alcantara Llaguno, S., Chen, J., Kwon, C.H., Jackson, E.L., Li, Y., Burns, D.K., Alvarez-Buylla, A., and Parada, L.F. (2009). Malignant astrocytomas originate from neural stem/progenitor cells in a somatic tumor suppressor mouse model. *Cancer Cell* 15, 45–56. <https://doi.org/10.1016/j.ccr.2008.12.006>.
31. Lee, J.H., Lee, J.E., Kahng, J.Y., Kim, S.H., Park, J.S., Yoon, S.J., Um, J.Y., Kim, W.K., Lee, J.K., Park, J., et al. (2018). Human glioblastoma arises from subventricular zone cells with low-level driver mutations. *Nature* 560, 243–247. <https://doi.org/10.1038/s41586-018-0389-3>.
32. Chen, F., and LoTurco, J. (2012). A method for stable transgenesis of radial glia lineage in rat neocortex by piggyBac mediated transposition. *J. Neurosci. Methods* 207, 172–180. <https://doi.org/10.1016/j.jneumeth.2012.03.016>.
33. Lee, Y., Messing, A., Su, M., and Brenner, M. (2008). GFAP promoter elements required for region-specific and astrocyte-specific expression. *Glia* 56, 481–493. <https://doi.org/10.1002/glia.20622>.
34. Brooks, L.J., Clements, M.P., Burden, J.J., Kocher, D., Richards, L., Devessa, S.C., Zakka, L., Woodberry, M., Ellis, M., Jaunmuktane, Z., et al. (2021). The white matter is a pro-differentiative niche for glioblastoma. *Nat. Commun.* 12, 2184. <https://doi.org/10.1038/s41467-021-22225-w>.
35. Picelli, S., Faridani, O.R., Björklund, A.K., Winberg, G., Sagasser, S., and Sandberg, R. (2014). Full-length RNA-seq from single cells using Smart-seq2. *Nat. Protoc.* 9, 171–181. <https://doi.org/10.1038/nprot.2014.006>.
36. Puchalski, R.B., Shah, N., Miller, J., Dalley, R., Nomura, S.R., Yoon, J.G., Smith, K.A., Lankovitch, M., Bertagnoli, D., Bickley, K., et al. (2018). An anatomic transcriptional atlas of human glioblastoma. *Science* 360, 660–663. <https://doi.org/10.1126/science.aaf2666>.
37. Yu, K., Hu, Y., Wu, F., Guo, Q., Qian, Z., Hu, W., Chen, J., Wang, K., Fan, X., Wu, X., et al. (2020). Surveying brain tumor heterogeneity by single-cell RNA-sequencing of multi-sector biopsies. *Natl. Sci. Rev.* 7, 1306–1318. <https://doi.org/10.1093/nsr/nwaa099>.
38. Miranda, A., Hamilton, P.T., Zhang, A.W., Pattnaik, S., Becht, E., Mezeheuski, A., Bruun, J., Micke, P., de Reynies, A., and Nelson, B.H. (2019). Cancer stemness, intratumoral heterogeneity, and immune response across cancers. *Proc. Natl. Acad. Sci. USA* 116, 9020–9029. <https://doi.org/10.1073/pnas.1818210116>.
39. Llorens-Bobadilla, E., Zhao, S., Baser, A., Saiz-Castro, G., Zwadlo, K., and Martin-Villalba, A. (2015). Single-cell transcriptomics reveals a population of dormant neural stem cells that become activated upon brain injury. *Cell Stem Cell* 17, 329–340. <https://doi.org/10.1016/j.stem.2015.07.002>.
40. Kalamakis, G., Brüne, D., Ravichandran, S., Bolz, J., Fan, W., Ziebell, F., Stiehl, T., Catalá-Martinez, F., Kupke, J., Zhao, S., et al. (2019). Quiescence modulates stem cell maintenance and regenerative capacity in the aging brain. *Cell* 176, 1407–1419.e14. <https://doi.org/10.1016/j.cell.2019.01.040>.
41. Mizrak, D., Levitin, H.M., Delgado, A.C., Crotet, V., Yuan, J., Chaker, Z., Silva-Vargas, V., Sims, P.A., and Doetsch, F. (2019). Single-cell analysis of regional differences in adult V-SVZ neural stem cell lineages. *Cell Rep.* 26, 394–406.e5. <https://doi.org/10.1016/j.celrep.2018.12.044>.
42. Dvorak, H.F. (1986). Tumors: wounds that do not heal. Similarities between tumor stroma generation and wound healing. *N. Engl. J. Med.* 315, 1650–1659.
43. Zhu, Q., Zhao, X., Zheng, K., Li, H., Huang, H., Zhang, Z., Mastracci, T., Wegner, M., Chen, Y., Sussel, L., and Qiu, M. (2014). Genetic evidence that Nkx2.2 and Pdgfra are major determinants of the timing of oligodendrocyte differentiation in the developing CNS. *Development* 141, 548–555. <https://doi.org/10.1242/dev.095323>.
44. Rowitch, D.H., and Kriegstein, A.R. (2010). Developmental genetics of vertebrate glial-cell specification. *Nature* 468, 214–222. <https://doi.org/10.1038/nature09611>.
45. Henrik Heiland, D., Ravi, V.M., Behringer, S.P., Frenking, J.H., Wurm, J., Joseph, K., Garrelfs, N.W.C., Strähle, J., Heynckes, S., Grauvogel, J., et al. (2019). Tumor-associated reactive astrocytes aid the evolution of immunosuppressive environment in glioblastoma. *Nat. Commun.* 10, 2541. <https://doi.org/10.1038/s41467-019-10493-6>.
46. Wang, Z., Xu, X., Liu, N., Cheng, Y., Jin, W., Zhang, P., Wang, X., Yang, H., Liu, H., and Tu, Y. (2018). SOX9-PDK1 axis is essential for glioma stem cell self-renewal and temozolomide resistance. *Oncotarget* 9, 192–204. <https://doi.org/10.18632/oncotarget.22773>.
47. Foudi, A., Hochedlinger, K., Van Buren, D., Schindler, J.W., Jaenisch, R., Carey, V., and Hock, H. (2009). Analysis of histone 2B-GFP retention reveals slowly cycling hematopoietic stem cells. *Nat. Biotechnol.* 27, 84–90. <https://doi.org/10.1038/nbt.1517>.
48. Basu, S., Dong, Y., Kumar, R., Jeter, C., and Tang, D.G. (2022). Slow-cycling (dormant) cancer cells in therapy resistance, cancer relapse and metastasis. *Semin. Cancer Biol.* 78, 90–103. <https://doi.org/10.1016/j.semcancer.2021.04.021>.
49. Deleyrolle, L.P., Harding, A., Cato, K., Siebzehnrubl, F.A., Rahman, M., Azari, H., Olson, S., Gabrielli, B., Osborne, G., Vescovi, A., and Reynolds, B.A. (2011). Evidence for label-retaining tumour-initiating cells in human glioblastoma. *Brain* 134, 1331–1343. <https://doi.org/10.1093/brain/awr081>.
50. Hoang-Minh, L.B., Siebzehnrubl, F.A., Yang, C., Suzuki-Hatano, S., Dajac, K., Loche, T., Andrews, N., Schmoll Massari, M., Patel, J., Amin, K., et al. (2018). Infiltrative and drug-resistant slow-cycling cells support metabolic heterogeneity in glioblastoma. *EMBO J.* 37, e98772. <https://doi.org/10.15252/emboj.201798772>.
51. Xie, X.P., Laks, D.R., Sun, D., Ganbold, M., Wang, Z., Pedraza, A.M., Bale, T., Tabar, V., Brennan, C., Zhou, X., and Parada, L.F. (2022). Quiescent human glioblastoma cancer stem cells drive tumor initiation, expansion, and

- p>recurrence following chemotherapy.
- Dev. Cell*
- 57, 32–46.e8.
- <https://doi.org/10.1016/j.devcel.2021.12.007>
- .
52. O'Connor, S.A., Feldman, H.M., Arora, S., Hoellerbauer, P., Toledo, C.M., Corrin, P., Carter, L., Kufeld, M., Bolouri, H., Basom, R., et al. (2021). Neural G0: a quiescent-like state found in neuroepithelial-derived cells and glioma. *Mol. Syst. Biol.* 17, e9522. <https://doi.org/10.15252/msb.20209522>.
 53. Müller, U., Steinhoff, U., Reis, L.F., Hemmi, S., Pavlovic, J., Zinkernagel, R.M., and Aguet, M. (1994). Functional role of type I and type II interferons in antiviral defense. *Science* 264, 1918–1921. <https://doi.org/10.1126/science.8009221>.
 54. Huang, S., Hendriks, W., Althage, A., Hemmi, S., Bluethmann, H., Kamijo, R., Vilcek, J., Zinkernagel, R.M., and Aguet, M. (1993). Immune response in mice that lack the interferon-gamma receptor. *Science* 259, 1742–1745. <https://doi.org/10.1126/science.8456301>.
 55. Ponti, G., Obernier, K., Guinto, C., Jose, L., Bonfanti, L., and Alvarez-Buylla, A. (2013). Cell cycle and lineage progression of neural progenitors in the ventricular-subventricular zones of adult mice. *Proc. Natl. Acad. Sci. USA* 110, E1045–E1054. <https://doi.org/10.1073/pnas.1219563110>.
 56. Calabrese, C., Poppleton, H., Kocak, M., Hogg, T.L., Fuller, C., Hamner, B., Oh, E.Y., Gaber, M.W., Finklestein, D., Allen, M., et al. (2007). A perivascular niche for brain tumor stem cells. *Cancer Cell* 11, 69–82. <https://doi.org/10.1016/j.ccr.2006.11.020>.
 57. Pollard, S.M., Yoshikawa, K., Clarke, I.D., Danovi, D., Stricker, S., Russell, R., Bayani, J., Head, R., Lee, M., Bernstein, M., et al. (2009). Glioma stem cell lines expanded in adherent culture have tumor-specific phenotypes and are suitable for chemical and genetic screens. *Cell Stem Cell* 4, 568–580. <https://doi.org/10.1016/j.stem.2009.03.014>.
 58. Hu, Y., and Smyth, G.K. (2009). ELDA: extreme limiting dilution analysis for comparing depleted and enriched populations in stem cell and other assays. *J. Immunol. Methods* 347, 70–78. <https://doi.org/10.1016/j.jim.2009.06.008>.
 59. Sharma, K., Schmitt, S., Bergner, C.G., Tyanova, S., Kannaiyan, N., Manrique-Hoyos, N., Kongi, K., Cantuti, L., Hanisch, U.K., Philips, M.A., et al. (2015). Cell type- and brain region-resolved mouse brain proteome. *Nat. Neurosci.* 18, 1819–1831. <https://doi.org/10.1038/nn.4160>.
 60. Townsend, D.M., and Tew, K.D. (2003). The role of glutathione-S-transferase in anti-cancer drug resistance. *Oncogene* 22, 7369–7375. <https://doi.org/10.1038/sj.onc.1206940>.
 61. Robertson, F.L., Marqués-Torrejón, M.A., Morrison, G.M., and Pollard, S.M. (2019). Experimental models and tools to tackle glioblastoma. *Dis. Model. Mech.* 12, dmm040386. <https://doi.org/10.1242/dmm.040386>.
 62. Richards, L.M., Whitley, O.K.N., MacLeod, G., Cavalli, F.M.G., Coutinho, F.J., Jaramillo, J.E., Svergun, N., Riverin, M., Croucher, D.C., Kuchida, M., et al. (2021). Gradient of developmental and injury response transcriptional states defines functional vulnerabilities underpinning glioblastoma heterogeneity. *Nat. Cancer* 2, 157–173.
 63. Ravi, V.M., Will, P., Kueckelhaus, J., Sun, N., Joseph, K., Salié, H., Vollmer, L., Kuliesiute, U., von Ehr, J., Benotmane, J.K., et al. (2022). Spatially resolved multi-omics deciphers bidirectional tumor-host interdependence in glioblastoma. *Cancer Cell* 40, 639–655.e13. <https://doi.org/10.1016/j.ccell.2022.05.009>.
 64. Dulken, B.W., Buckley, M.T., Navarro Negredo, P., Saligrama, N., Cayrol, R., Leeman, D.S., George, B.M., Boutet, S.C., Hebestreit, K., Pluvinaige, J.V., et al. (2019). Single-cell analysis reveals T cell infiltration in old neurogenic niches. *Nature* 571, 205–210. <https://doi.org/10.1038/s41586-019-1362-5>.
 65. Gangoso, E., Southgate, B., Bradley, L., Rus, S., Galvez-Cancino, F., McGivern, N., Güç, E., Kapourani, C.A., Byron, A., Ferguson, K.M., et al. (2021). Glioblastomas acquire myeloid-affiliated transcriptional programs via epigenetic immunoevasion to elicit immune evasion. *Cell* 184, 2454–2470.e26. <https://doi.org/10.1016/j.cell.2021.03.023>.
 66. Liu, Y., Lv, J., Liu, J., Liang, X., Jin, X., Xie, J., Zhang, L., Chen, D., Fiske-sund, R., Tang, K., et al. (2018). STAT3/p53 pathway activation disrupts IFN-beta-induced dormancy in tumor-repopulating cells. *J. Clin. Invest.* 128, 1057–1073. <https://doi.org/10.1172/JCI96329>.
 67. Liu, Y., Liang, X., Yin, X., Lv, J., Tang, K., Ma, J., Ji, T., Zhang, H., Dong, W., Jin, X., et al. (2017). Blockade of l-tryptophan-kynurenine-AhR metabolic circuitry abrogates IFN-gamma-induced immunologic dormancy of tumor-repopulating cells. *Nat. Commun.* 8, 15207. <https://doi.org/10.1038/ncomms15207>.
 68. Farrar, J.D., Katz, K.H., Windsor, J., Thrush, G., Scheuermann, R.H., Uhr, J.W., and Street, N.E. (1999). Cancer dormancy. VII. A regulatory role for CD8+ T cells and IFN-gamma in establishing and maintaining the tumor-dormant state. *J. Immunol.* 162, 2842–2849.
 69. Correia, A.L., Guimaraes, J.C., Auf der Maur, P., De Silva, D., Trefny, M.P., Okamoto, R., Bruno, S., Schmidt, A., Mertz, K., Volkmann, K., et al. (2021). Hepatic stellate cells suppress NK cell-sustained breast cancer dormancy. *Nature* 600, E7. <https://doi.org/10.1038/s41586-021-03614-z>.
 70. Varn, F.S., Johnson, K.C., Martinek, J., Huse, J.T., Nasrallah, M.P., Wesseling, P., Cooper, L.A.D., Malta, T.M., Wade, T.E., Sabedot, T.S., et al. (2022). Glioma progression is shaped by genetic evolution and microenvironment interactions. *Cell* 185, 2184–2199.e16. <https://doi.org/10.1016/j.cell.2022.04.038>.
 71. Bansal, R., Warrington, A.E., Gard, A.L., Ranscht, B., and Pfeiffer, S.E. (1989). Multiple and novel specificities of monoclonal antibodies O1, O4, and R-mAb used in the analysis of oligodendrocyte development. *J. Neurosci. Res.* 24, 548–557. <https://doi.org/10.1002/jnr.490240413>.
 72. Marino, S., Vooijs, M., van Der Gulden, H., Jonkers, J., and Berns, A. (2000). Induction of medulloblastomas in p53-null mutant mice by somatic inactivation of Rb in the external granular layer cells of the cerebellum. *Genes Dev.* 14, 994–1004.
 73. Pathania, M., De Jay, N., Maestro, N., Harutyunyan, A.S., Nitarska, J., Pahlavan, P., Henderson, S., Mikael, L.G., Richard-Londt, A., Zhang, Y., et al. (2017). H3.3(K27M) cooperates with Trp53 loss and PDGFRA gain in mouse embryonic neural progenitor cells to induce invasive high-grade gliomas. *Cancer Cell* 32, 684–700.e9. <https://doi.org/10.1016/j.ccell.2017.09.014>.
 74. Schneider, C.A., Rasband, W.S., and Eliceiri, K.W. (2012). NIH Image to ImageJ: 25 years of image analysis. *Nat. Methods* 9, 671–675. <https://doi.org/10.1038/nmeth.2089>.
 75. Butler, A., Hoffman, P., Smibert, P., Papalexi, E., and Satija, R. (2018). Integrating single-cell transcriptomic data across different conditions, technologies, and species. *Nat. Biotechnol.* 36, 411–420. <https://doi.org/10.1038/nbt.4096>.
 76. Bankhead, P., Loughrey, M.B., Fernández, J.A., Dombrowski, Y., McArt, D.G., Dunne, P.D., McQuaid, S., Gray, R.T., Murray, L.J., Coleman, H.G., et al. (2017). QuPath: open source software for digital pathology image analysis. *Sci. Rep.* 7, 16878. <https://doi.org/10.1038/s41598-017-17204-5>.
 77. Kuhn, M. (2008). Building predictive models in R using the caret package. *J. Stat. Softw.* 28.
 78. Bates, D., Mächler, M., Bolker, B., and Walker, S. (2015). Fitting linear mixed-effects models using lme4. *J. Statistical Software* 67, 48. <https://doi.org/10.18637/jss.v067.i01>.
 79. Krimpenfort, P., Quon, K.C., Mooi, W.J., Loonstra, A., and Berns, A. (2001). Loss of p16Ink4a confers susceptibility to metastatic melanoma in mice. *Nature* 413, 83–86. <https://doi.org/10.1038/35092584>.
 80. Feliciano, D.M., Lafourcade, C.A., and Bordey, A. (2013). Neonatal sub-ventricular zone electroporation. *J. Vis. Exp.* <https://doi.org/10.3791/50197>.
 81. Ottone, C., Krusche, B., Whitby, A., Clements, M., Quadrato, G., Pitulescu, M.E., Adams, R.H., and Parrinello, S. (2014). Direct cell-cell contact with the vascular niche maintains quiescent neural stem cells. *Nat. Cell Biol.* 16, 1045–1056. <https://doi.org/10.1038/ncb3045>.
 82. Kim, H., Kim, E., Park, M., Lee, E., and Namkoong, K. (2013). Organotypic hippocampal slice culture from the adult mouse brain: a versatile tool for

- translational neuropsychopharmacology. *Prog. Neuro-Psychopharmacol. Biol. Psychiatry* 41, 36–43. <https://doi.org/10.1016/j.pnpbp.2012.11.004>.
83. Lim, J.F., Berger, H., and Su, I.H. (2016). Isolation and activation of murine lymphocytes. *J. Vis. Exp.* <https://doi.org/10.3791/54596>.
84. Zuckermann, M., Hovestadt, V., Knobbe-Thomsen, C.B., Zapatka, M., Northcott, P.A., Schramm, K., Belic, J., Jones, D.T.W., Tschida, B., Moriarity, B., et al. (2015). Somatic CRISPR/Cas9-mediated tumour suppressor disruption enables versatile brain tumour modelling. *Nat. Commun.* 6, 7391. <https://doi.org/10.1038/ncomms8391>.
85. Weber, J., Öllinger, R., Friedrich, M., Ehmer, U., Barenboim, M., Steiger, K., Heid, I., Mueller, S., Maresch, R., Engleitner, T., et al. (2015). CRISPR/Cas9 somatic multiplex-mutagenesis for high-throughput functional cancer genomics in mice. *Proc. Natl. Acad. Sci. USA* 112, 13982–13987. <https://doi.org/10.1073/pnas.1512392112>.
86. Beronja, S., Livshits, G., Williams, S., and Fuchs, E. (2010). Rapid functional dissection of genetic networks via tissue-specific transduction and RNAi in mouse embryos. *Nat. Med.* 16, 821–827. <https://doi.org/10.1038/nm.2167>.
87. McInnes, L., Healy, J., and Melville, J. (2018). UMAP: uniform manifold approximation and projection for dimension reduction. Preprint at arXiv. <https://doi.org/10.48550/arXiv.1802.03426>.
88. Marco-Sola, S., Sammeth, M., Guigó, R., and Ribeca, P. (2012). The GEM mapper: fast, accurate and versatile alignment by filtration. *Nat. Methods* 9, 1185–1188. <https://doi.org/10.1038/nmeth.2221>.
89. Waltman, L., and van Eck, N.J. (2013). A smart local moving algorithm for large-scale modularity-based community detection. *Eur. Phys. J. B* 86, 471. <https://doi.org/10.1140/epjb/e2013-40829-0>.
90. Hardoon, D.R., Szedmak, S., and Shawe-Taylor, J. (2004). Canonical correlation analysis: an overview with application to learning methods. *Neural Comput.* 16, 2639–2664. <https://doi.org/10.1162/0899766042321814>.
91. Mereu, E., Lafzi, A., Moutinho, C., Ziegenhain, C., McCarthy, D.J., Álvarez-Varela, A., Batlle, E., Sagar Grun, D., Grün, D., Lau, J.K., et al. (2020). Benchmarking single-cell RNA-sequencing protocols for cell atlas projects. *Nat. Biotechnol.* 38, 747–755. <https://doi.org/10.1038/s41587-020-0469-4>.
92. Maley, C.C., Koelble, K., Natrajan, R., Aktipis, A., and Yuan, Y. (2015). An ecological measure of immune-cancer colocalization as a prognostic factor for breast cancer. *Breast Cancer Res.* 17, 131. <https://doi.org/10.1186/s13058-015-0638-4>.
93. Golay, J., Kanevski, M., Vega Orozco, C.D., and Leuenberger, M. (2014). The multipoint Morisita index for the analysis of spatial patterns. *Physica A Statistical Mechanics and its Applications* 406, 191–202. <https://doi.org/10.1016/j.physa.2014.03.063>.

STAR★METHODS

KEY RESOURCES TABLE

REAGENT or RESOURCE	SOURCE	IDENTIFIER
Antibodies		
rabbit anti-cleaved caspase 3 (Asp175) (5A1E)	Cell Signalling Technology	Cat#9664; RRID:AB_2070042
rat monoclonal anti-CD68 (clone FA-11)	Abcam	Cat#ab53444; RRID:AB_869007
rabbit polyclonal anti-RFP	Antibodies-online	Cat#ABIN129578; RRID:AB_10781500
anti-O4 antibody	Bansal et al. ⁷¹	RRID:AB_357617
rabbit anti-Sox2	Abcam	Cat# ab97959; RRID:AB_2341193
rabbit polyclonal anti-GFAP	Dako	Cat#Z0334; RRID:AB_10013382
rabbit polyclonal anti-Olig2	Millipore	Cat#AB9610; RRID:AB_570666
rabbit polyclonal anti-red fluorescent protein (RFP)	Antibodies online	Cat# ABIN129578; RRID:AB_10781500
goat polyclonal anti-human Sox9	R and D systems	Cat# AF3075; RRID:AB_2194159
rat polyclonal anti-CD45 (Leukocyte common antigen, Ly-5)	BD Biosciences	Cat#550539; RRID:AB_2174426
rabbit polyclonal anti-Iba1	FUJIFILM Wako Shibayagi	Cat#019-19741; RRID:AB_839504
rat monoclonal anti-CD8a	Thermo Fisher Scientific	Cat#14-0808-82; RRID:AB_2572861
rat monoclonal anti-CD4	BD Biosciences	Cat#550280; RRID:AB_393575
goat polyclonal anti-mouse Nkp46	R and D systems	Cat#AF2225; RRID:AB_355192
rat monoclonal anti-CD31 platelet endothelial cell adhesion molecule (PECAM)	BD Biosciences	Cat#550274; RRID:AB_393571
rabbit polyclonal anti-doublecortin (DCX)	Abcam	Cat#ab18723; RRID:AB_732011
mouse polyclonal anti-GFAP	Abcam	Cat#ab18723; RRID:AB_732011
rat monoclonal anti-CD44 (Clone KM114)	BD Biosciences	Cat#558739; RRID:AB_397098
rabbit polyclonal anti-luciferase	Merck	Cat#L0159; RRID:AB_260379
rabbit monoclonal anti-Cdkn2a/p16INK4a	Abcam	Cat#ab211542; RRID:AB_2891084
rabbit polyclonal anti-p53	Novocastra Leica	Cat# NCL-L-p53-CM5p; RRID:AB_2895247
goat polyclonal mouse pdgfra	R & D Systems	Cat#AF1062; RRID:AB_2236897
rabbit polyclonal anti NF1	Thermo Fisher	Cat#A300-140A-M; RRID:AB_2779035
rabbit monoclonal anti-Pten	Cell signaling	Cat#sc-9559; RRID:AB_390810
rabbit polyclonal anti-Egfr	Millipore	Cat#06847; RRID:AB_2096607
mouse monoclonal anti-Gapdh	Abcam	Cat#ab8245; RRID:AB_2107448
InVivoMAb rat, anti-mouse CD16/CD32	Bio X Cell	Cat#BE0307; RRID:AB_2736987
MS CD45 BUV563 30-F11	BD Biosciences	Cat#612924; RRID:AB_2870209
BUV661 rat anti-CD11b	BD Biosciences	Cat#565080; RRID:AB_2722548
Ms Bta 2 Mgcobn BC BUV805 S19.8	BD Biosciences	Cat#749215; RRID:AB_2873593
Brilliant violet 510 TM anti-mouse H-2Kb	BioLegend	Cat#116523; RRID:AB_2800584
CD317 (BST2)	BD Biosciences	Cat#747605; RRID:AB_2744173
I-A/I-E	BD Biosciences	Cat#563414; RRID:AB_2738191
CD74	BD Biosciences	Cat#740274; RRID:AB_2740014
Ki67 monoclonal antibody (SolA15), eFluor TM 450, eBioscience	Thermo Fisher	Cat#48-5698-80; RRID:AB_11151155
Brilliant violet 650 TM anti-mouse CD317 (BST2, PDCA-1)	Biolegend	Cat#127019; RRID:AB_2562477
Brilliant violet 785 TM anti-mouse/human CD44	Biolegend	Cat#103059; RRID:AB_2571953
Purified anti-GFP	Biolegend	Cat#338001; RRID:AB_1279415

(Continued on next page)

Continued

REAGENT or RESOURCE	SOURCE	IDENTIFIER
NK-1.1	BD Biosciences	Cat#564144; RRID:AB_2738618
BUV496 rat anti-mouse CD4	BD Biosciences	Cat#564667; RRID:AB_2722549
rat monoclonal anti-CD3	BD Biosciences	Cat#564380; RRID:AB_2738781
BUV805 rat anti-mouse CD8a	BD Biosciences	Cat#564920; RRID:AB_2716856
FoxP3 monoclonal antibody (FJK-16s), eFluor™450, eBioscience	Thermo Fisher	Cat#48-5773-82; RRID:AB_1518812
Chemicals, peptides, and recombinant proteins		
Doxycycline	Sigma	Cat#PHR437
Temozolomide	Sigma	Cat#F7258
Fast green	Sigma	Cat#P6148
EdU	Insight Biotechnology	Cat#sc-284628A
Triton X-100	Merck	Cat#RES9690T-A102X
DAPI	Insight Biotechnology	Cat#sc-3598
SYTOX green	Thermo Fisher	Cat#S7020
Prolong gold antifade reagent	Thermo Fisher	Cat#P36964
Papain dissociation DNase vial	Worthington	Cat#LK003172
Papain dissociation papain vial	Worthington	Cat#LK003178
DMEM/F12	Thermo Fisher	Cat#11320074
N2 supplement	Thermo Fisher	Cat#17502001
B27 (- vitamin A) supplement	Thermo Fisher	Cat#12587010
FGF	Preprotech	Cat#450-33A
EGF	Preprotech	Cat# 315-09-1000
Laminin	Sigma	Cat#L2020
Kanamycin sulfate	VWR	Cat#420411
Gentamycin	Fisher Scientific	Cat#11470435
Non-essential amino acids	Thermo Fisher	Cat#11140035
Beta-mercaptoethanol	Thermo Fisher	Cat#31350010
Bovine serum albumin	Thermo Fisher	Cat#15260-037
L-Glucose	Sigma	Cat#G8769
Accutase	Biolegend	Cat#423201
Neurobasal medium	Thermo Fisher	Cat#21103-049
L-glutamine	Thermo Fisher	Cat#25030081
RPMI 1640	Merck	Cat#R8758
Mojo buffer	Biolegend	Cat#480017
TexMACs media	Miltenyi Biotech	Cat#130-097-196
IL-2	Preprotech	Cat#AF-212-12-5
Dynabeads mouse T activator CD3/CD8	GIBCO	Cat#11456D
Interferon β	R & D systems	Cat#8234-MB-010
Interferon γ	Preprotech	Cat#315-05-20
RIPA buffer	Sigma	Cat#P8340
Phosphatase inhibitor cocktail II	Sigma	Cat#P5726
Phosphatase inhibitor cocktail III	Sigma	Cat#P0044
Luminata classico	Millipore	Cat#WBLUC0500
Luminata crescendo	Millipore	Cat#WBLUR0500
Liberase TL	Roche	Cat#05401119001
DNAse1	Merck	Cat#10104159001
eBioscience fixable viability dye eFluor™ 780	Thermo Fisher	Cat#65-0865-18
Myelin removal beads	Miltenyi Biotech	Cat#130-096-731

(Continued on next page)

Continued

REAGENT or RESOURCE	SOURCE	IDENTIFIER
RNAse inhibitor	Takara Bio	Cat#2313A
Superscript II	Thermo Fisher	Cat#18064014
Betaine	Sigma	Cat# 61962
KAPA HiFi hotstart ready mix	Kapa Biosystems	Cat#KK2601
AMPure XP beads	Beckman Coulter	Cat#A63881
Agilent high sensitivity DNA kit	Agilent	Cat#5067-4628
SPRIselect beads	Beckman Coulter	Cat#B23317

Critical commercial assays

Click-IT EdU Alexa Fluor 647 Flow Cytometry Assay kit	Invitrogen	Cat#C10419
Click-IT™ EdU Alexa Fluor™ 647 Imaging kit	Invitrogen	Cat#C10340
InFusion cloning kit	Clontech	Cat#638917
Cytofix/Cytoperm solution kit	BD biosciences	Cat#554714
eBioscience™ FoxP3/transcription factor staining buffer set	Thermo fisher	Cat#00-5523-00
Nextera XT DNA library preparation kit	Illumina	Cat#FC-131-1096
Nextera XT index kit	Illumina	Cat#FC-131-1001
Chromium Next GEM Single Cell 3' Kit v3.1	10X Genomics	Cat#1000269
CD3 T cell negative isolation kit	Biolegend	Cat#480023

Deposited data

Yu et al. scRNA seq dataset	Yu et al. ³⁷	GEO: GSE117891
IVY glioblastoma atlas project	https://glioblastoma.alleninstitute.org/static/download.html	RRID:SCR_005044
Chinese Glioma Genome Atlas (CGGA)	N/A	RRID:SCR_018802
The Cancer Genome Atlas (TCGA)	N/A	RRID:SCR_003193
single-cell RNA data (bulk/margin)	This publication	GEO:GSE174470
single-cell RNA data (H2B-GFP ⁺ /H2B-GFP ⁻)	This publication	GEO:GSE228785

Experimental models: Organisms/strains

Mouse: Cdkn2a ^{fl/fl} mice	N/A	MGI:2384163
Mouse: p53 ^{fllox/flox} ; Trp53 ^{tm1Bm}	Marino et al. ⁷²	MGI:1931011
Mouse: <i>Ifnar1</i> ^{-/-}	N/A	MGI:1930950
Mouse: <i>Ifnar1</i> ^{-/-} ; <i>ifngr1</i> ^{-/-}	Jax mice 029098	RRID: IMSR_JAX:029098
Mouse: C57Bl/6J	Jax mice 000664	RRID:ISMR_JAX:000664

Recombinant DNA

Plasmid: pAAV-GFAP-EGFP	Roth lab	Addgene plasmid #50743; RRID:Addgene_50743
Plasmid: pBOB-CAG-iCRE-SD	Inder Verma	Addgene#12336
Plasmid: pCAG-PBase	Pathania et al. ⁷³	N/A
Plasmid: EF1a-TdTomato-CAG-Pdgfr (D842V)	Pathania et al. ⁷³	N/A
Plasmid: pCW57.1	David Root	Addgene plasmid#41393; RRID:Addgene_41393
Plasmid: LV-GFP	Elaine Fuchs	Addgene plasmid#25999; RRID:Addgene_25999

Software and algorithms

Fiji ImageJ.0	Schneider et al. ⁷⁴	RRID:SCR_003070
Snapgene	N/A	RRID: SCR_015052
Flowjo v10.7.1	N/A	RRID:SCR_008520
CellRanger v3.1.0	10x Genomics	RRID:SCR_023221
Seurat v4.0.3	Butler et al. ⁷⁵	RRID:SCR_007322
QuPath	Bankhead et al. ⁷⁶	RRID:SCR_018257
caret	Khun et al. ⁷⁷	RRID:SCR_021138
R package lme4	Bates et al. ⁷⁸	RRID:SCR_015654
GraphPad Prism	N/A	RRID:SCR_002798

RESOURCE AVAILABILITY

Lead contact

Further information and requests for resources and reagents should be directed to and will be fulfilled by the lead contact, Simona Parrinello (simona.parrinello@ucl.ac.uk).

Materials availability

All unique/stable reagents generated in this study are available from the [lead contact](#) with a completed materials transfer agreement.

Data and code availability

- Single-cell RNA-seq data have been deposited at GEO. Accession numbers are listed in the [key resources table](#).
- This paper does not report original code.
- Any additional information required to reanalyse the data reported in this paper is available from the [lead contact](#) upon request.

EXPERIMENTAL MODEL AND STUDY PARTICIPANT DETAILS

All procedures were performed in compliance with the Animal Scientific Procedures Act, 1986 and approved by the UCL Animal Welfare and Ethical Review Body (AWERB) in accordance with the international guidelines of the Home Office (UK). *Trp53^{fl/fl}* mice were obtained from the Jackson Laboratory (*Trp53^{tm1Bm/J}*; Jax 008462)⁷² and *Cdkn2a^{fl/fl}* mice were provided by A. Berns (*Cdkn2a^{atm2Bm/A}*).⁷⁹ *Trp53^{fl/fl}* pups were used for modeling Nf1 and Pdgfr tumor models, *Cdkn2a^{fl/fl}* mice were used for the EGFR model. Wildtype C57BL6/J mice were purchased from Charles River and used for the EGFR-H2B-GFP model. *Ifnar1^{-/-}* and *Ifngr1^{-/-}*; *Ifnar1^{-/-}* mouse lines were provided by Michel Aguet.^{53,54} Female and male mice were used for tumor modeling at either postnatal day 2 for somatic models or 8–12 weeks of age for orthotopic models. Mice were monitored daily and sacrificed when they began to show signs of disease and reached humane endpoints. These were 50–112 days for the somatic models, for the GFP⁺/GFP⁻ reinjection study this was 56–58 days and 29–33 days respectively, and for the bulk compared to margin reinjection study this was between 43–53 days and 57–88 days respectively. To study the distribution of GSCs between bulk and margin, EdU (50 mg/kg; Insight Biotech, sc-284628A) was injected 2 h prior to sacrifice to label rapidly dividing cells in the brain. To identify dormant tumor cells in the EGFR-H2B-GFP model, doxycycline (Sigma, D891) was administered through the drinking water (0.2% doxycycline:1% sucrose) immediately following plasmid injection. Doxycycline withdrawal was carried out for a minimum of 2 weeks to dilute the H2B-GFP reporter in actively cycling cells. For temozolomide treatment, Pdgfr tumor mice were given i.p. injections of temozolomide (Sigma PHR437) 100 mg/kg (prepared in 10% DMSO and saline) at six weeks post-electroporation for 5 days, before collection of brains following perfusion under terminal anesthesia 3 days later.

METHOD DETAILS

In vivo electroporation

Plasmids were injected into the ventricle of isoflurane-immobilized pups at postnatal day 2 using an Eppendorf Femtojet microinjector (Eppendorf, 5247000030), followed by electroporation (5 square pulses, 50 msec/pulse at 100V, with 850 msec intervals).⁸⁰ PiggyBase (0.5 µg/µl) and PiggyBac vectors at a molar ratio of 1:1 were diluted in saline (0.9% NaCl) containing 0.1% fast green (Sigma, F7258).

Orthotopic injections

For analysis of tumorigenicity of GFP⁺ and GFP⁻ populations stereotaxic injections of 1×10^5 primary tumor cells derived from EGFR tumors were performed in 8-week-old female C57BL6/J mice. For T cell depletion experiments, stereotaxic injections of 2×10^5 primary tumor cells derived from EGFR tumors were performed in 8-week-old female CD-1 nude mice and heterozygous littermate controls. For analysis of bulk versus margin, stereotaxic injections of 0.5×10^5 primary tumor cells derived from Pdgfr tumors were performed in 8–12-week-old female C57BL6/J mice. Co-ordinates: anteroposterior 0, mediolateral -2.25, dorsoventral -3. Animals were sacrificed and tumors collected when they showed signs of distress or >10% weight loss. For T cell experiments tumors were collected at 2 weeks post-implantation. To assess tumor cell proliferation EdU was administered by i.p. injection (50 mg/kg) 2 h prior to collection. Survival was analyzed using the Kaplan–Meier method and significance calculated using the log rank Mantel–Cox test.

Tissue preparation and immunohistochemistry

Animals were perfused (4% paraformaldehyde in PBS; Merck P6148) under terminal anesthesia, brains collected and post-fixed overnight at 4°C in PFA (4%). Vibratome sections (50 µm) were prepared and stored in cryopreservative (glycerol:ethylene glycol; PBS 1:1:2) prior to immunohistochemistry. For staining, floating sections were permeabilized overnight (1% Triton X-100, 10% serum in PBS) at 4°C, incubated in primary antibody overnight (1% Triton X-100, 10% serum in PBS) at 4°C and for 3 h in secondary antibody

(0.5% Triton X-100, 10% serum in PBS) at room temperature. Sections were counterstained with DAPI (Insight Biotechnology, sc-3598) for 10 min at room temperature and mounted with antifade mounting solution (Prolong gold antifade mountant, Thermo Fisher, P36934).

Organotypic slices were fixed overnight at 4°C (4% paraformaldehyde in PBS), blocked and permeabilized for 48 h at 4°C (3% Triton X-100, 10% serum in PBS), incubated with primary antibody for 48 h at 4°C (0.5% Triton X-100, 10% serum in PBS), washed 3 × 2hr and incubated overnight in secondary antibody (0.5% Triton X-100, 10% serum in PBS). Sections were washed 3 × 2hr and counterstained with SYTOX Green (Thermo Fisher, S7020) for 2 h at room temperature and mounted with antifade mounting solution (Thermo Fisher, P36964).

For *in vitro* immunofluorescence, cells were fixed in 4% PFA, permeabilized in 0.5% Triton X-100 and blocked in 10% serum in PBS then incubated with primary antibody overnight at 4°C in PBS +10% serum. Anti-O4 antibody (1:100 hybridoma supernatant IgM⁷¹) staining was performed on live cells for 30 min at 37°C in cell culture media. Secondary antibodies were diluted in 10% serum in DAPI (1:10000 in PBS) and incubated at RT for 1 h. Coverslips were mounted with antifade mounting solution. Imaging was carried out using the Zeiss Z1 upright microscope or the Zeiss LSM880 confocal microscope. Quantification was performed using Fiji ImageJ.0 (RRID:SCR_003070).

The following antibodies were used: rabbit anti-Sox2 (1:500; Abcam, ab97959), rabbit anti-GFAP (1:1,000; Dako, Z0334), rabbit anti-Olig2 (1:500; Millipore, ab9610), rabbit anti-RFP (1:1000; Antibodies Online, ABIN129578), goat anti-Sox9 (1:500; AF3075), rat anti-CD45 (1:500; BD, 550539), rat anti-CD68 (1:500; Abcam, ab53444), rabbit anti-Iba1 (1:1,000; Wako, 019-19741), rat anti-CD8a (1:250; 14-0808-82), rat anti-CD4 (1:100; BD, 550280), goat anti-Nkp46 (1:250; R&D, af2225), rat anti-CD31 (1:500; BD, 550274), rabbit anti-DCX (1:1000; abcam, ab18723), goat anti-GFAP (1:500 (organotypic sections) or 1:2000 (coverslips), abcam, ab53554), mouse anti-O4 (1:100 hybridoma supernatant IgM⁷¹), rat anti-Mouse CD44 (1:500; BD, 558739), rabbit anti-luciferase (1:500; Sigma, L0159). For detection of EdU, sections were stained with Click-it EdU Alexa Fluor 647 Imaging Kit (Invitrogen, C10340) following manufacturer guidelines. For histopathology assessment, brains were post-fixed in 10% formalin overnight before tissue processing and paraffin embedding. 3μm sections were cut and stained with hematoxylin and eosin using standard methods.

Derivation and culture of cell lines

Neural stem cells were isolated from *Trp53*^{fl/fl} and *Cdkn2a*^{fl/fl} pups as previously described.⁸¹ Briefly, pup brains (P9-14) were collected, and the lateral ventricles dissected out. Neural stem cells were isolated by enzymatic digestion using Papain dissociation (Worthington, LK003178/LK003172). Cells were seeded in NSC media (DMEM/F12 supplemented with N2 (1x), B27 lacking retinoic acid (1x), kanamycin (100 mg/mL)/gentamycin (2 mg/mL), heparin (4 mg/mL), FGF (10 ng/mL) and EGF (20 ng/mL) and expanded as neurospheres for one passage prior to plating on laminin-coated (1:200 in PBS) plates and cultured adherently in serum-free GSC media (N2 (1/200), B27 (1/100) (Life Technologies), 1 mg/mL laminin (Sigma), 10 ng/mL EGF and FGF-2 (Peprotech), 1 × MEM NEAA (Gibco), 0.1 mM betamercaptoethanol, 0.012% BSA (Gibco), 0.2 g/L glucose (Sigma), 1000 U/ml penicillin-streptomycin (Sigma)).⁵⁷ For preparation of tumor cell lines, brains from tumor-bearing animals were collected into ice-cold HBSS media. Under fluorescence guidance, tdTomato⁺ tumor regions were microdissected, enzymatically digested and cultured as described above, with the exception of EGFR tumor-derived cells which were maintained and subcultured as neurospheres. Medium was changed every 3 d, and cells were dissociated using Accutase solution (Sigma). For experiments involving assessment of proliferation, cells were exposed to 10 μm EdU prior to collection. For differentiation experiments, 5 × 10⁴ cells were seeded on glass coverslips and cultured without EGF or FGF for 5 days.

Regional injection of tumor-derived cells into organotypic tumor slices

Animals were sacrificed by cervical dislocation and tumor-bearing brains were sectioned on a Leica Vibratome (VT 1200S) at 200 μm on ice in HBSS (supplemented with kanamycin/gentamycin) and transferred to a 6 well plate containing MillicellTM Culture plate inserts of 0.4 μm pore size (Thermo Scientific, 10094680) in 1 mL of Neurobasal complete media, supplemented with 2% B27 (Thermo Fisher, 17504-044), 2 mM L-Glutamine (Gibco, 3505006) and kanamycin (100 mg/mL)/gentamycin (2 mg/mL), and incubated overnight (5% CO₂ 37°C).⁸² Tumor derived Nf1 cells (passage 2) engineered to express mtagBFP2 and luciferase were microinjected into the bulk of the tdTomato⁺ tumor and the contralateral hemisphere of each slice. Injected slices were cultured for 5 days with media changed every 2 days and then fixed and processed for immunohistochemistry as described above.

T cell isolation from spleen and glioma-T cell co-culture

Spleens were harvested from 6 to 10-week-old C57BL/6/J mice into ice-cold RPMI-1640 media (Sigma, R8758) supplemented with 2% Fetal Bovine Serum (Sigma, F7524). A single cell suspension of splenocytes was obtained by gently mincing the spleen with the flat end of a syringe's plunger, in ice-cold 2% FBS RPMI media.⁸³ Dissociated splenocytes were filtered through a 70 μm filter and centrifuged for 5 min at 300 g at 4°C. The cell pellet was resuspended in 5 mL of PBS (Ca/Mg free) and centrifuged again. Cells were resuspended in up to 4 mL of freshly prepared 1x Mojo Buffer (Biolegend, 480017) and untouched CD3 T cells were isolated using a commercial mouse CD3 T cell negative isolation kit (Biolegend, 480023), following the manufacturer's instructions.

For co-culture experiments, 2,000 primary tumor cells isolated from EGFR tumors were seeded on laminin-coated 24 well-plate wells and cultured overnight in complete hGSC media to allow them to adhere. The following day, the media was replaced with serum-free TexMACs media (Miltenyi, 130-097-196) supplemented with EGF (20 ng/mL), FGF (10 ng/mL), Laminin (2 μg/mL), murine

IL-2 (5 ng/mL; Peprotech, AF-212-12-5) and Dynabeads mouse T-Activator CD3/CD28 (at a 1:1 T cell ratio, as indicated by the supplier; Gibco, 11456D) in the absence (for alone control) or presence of 10,000 T cells (for co-culture). EdU was added 22 h later and cells were collected at 24h. The Click-iT EdU Alexa Fluor 647 Flow Cytometry Assay Kit (Invitrogen, C10419) was used to detect cells in S phase, following manufacturer's instructions. Cells were stained with DAPI (1:10,000 in PBS) and acquired on a BD Fortessa X20 Flow cytometer for analysis.

Interferon treatment and cell proliferation assay

Primary tumor cells were isolated from EGFR-H2B-GFP tumors and cultured as neurospheres as above. Cells were incubated in the presence or absence of interferon β (1,000 U/ml; R&D, 8234-MB-010), interferon γ (1,000 U/ml; Peprotech, 315-05-20) or both combined for 48 h. EdU (10 μ M) was added to the media 2 h prior to collection to label dividing cells. Following EdU labeling (10 μ M; Invitrogen, C10424) according to the manufacturer's instructions, a minimum of 10,000 cells were analyzed using a BD LSRFortessa X-20 Flow Cytometer and cell-cycle profiles measured using FlowJo software.

Cell migration assay

Primary tumor cells were isolated from Pdgfr tumors and cultured as above. Cells were incubated in the presence or absence of interferon γ (1,000 U/ml; Peprotech, 315-05-20). Live cell imaging was conducted using the Incucyte SX5. Cells were tracked manually in ImageJ using the ManualTracking plugin.

Clonogenicity assay

Tumorspheres were dissociated using accutase and seeded in wells of a 96 well plate in decreasing concentrations from 50 to 1 cell per well. Wells containing at least one sphere were scored as positive after two weeks of culture. A total of 16 wells were scored for each condition. Quantitative and statistical analysis was performed at <http://bioinf.wehi.edu.au/software/elda>.⁵⁸

Western blot

GBM mutations were verified on tumor derived and NSC cell lines by Western blotting. Protein lysates were prepared in RIPA buffer (containing protease (1:100; Sigma, P8340) and phosphatase inhibitors (1:500; Sigma, P5726 and P0044). Western Blots were performed following standard protocols. Membranes were incubated with primary antibodies in 5% milk in TBST (TBS+ 0.05% Tween) overnight at 4°C, washed and incubated in secondary antibody (in 5% milk in TBST) at room temperature for 1h. Proteins were detected using Luminata Crescendo (Millipore, WBLUR0500) or Classico (Millipore, WBLUC0500) Western HRP reagents and imaged using the ImageQuant system.

The following primary antibodies were used: rabbit anti-p16 (1:500; Abcam, ab211542), rabbit anti-Trp53 (1:500; Novocastra Leica, NCL-L-p53-CM5P), goat anti-Pdgfra (1:500; R&D, AF1062), rabbit anti-Nf1 (1:1,000; Bethyl, A300-140A-M), rabbit anti-Pten (1:1,000, Cell Signaling, 9559), rabbit anti-EGFR (1:1,000; Millipore, 06847) and mouse anti-Gapdh (1:5,000; Abcam, ab8245). HRP secondary antibodies were purchased from ThermoFisher.

Plasmid generation

Constructs were generated using InFusion Kit (Clontech, 638917) and T4 DNA Ligase (NEB, M0202S), following manufacturer's instructions. Plasmids were transformed in chemically competent bacteria strains Top10 (Thermo Fisher, C303003) and Stbl3 (Thermo Fisher, C737303). Stbl3 bacteria strain was used for PiggyBac vectors to minimize recombination. Plasmid construction and verification of constructs was designed using Snapgene software (RRID: SCR_015052). Previously described sgRNA were used to target *Pten* and *Nf1*⁸⁴ for the Nf1 model and the *Cdkn2a* locus for the EGFR-H2B-GFP model.⁸⁵

PiggyBases

The hGFAP_{MIN}-PBase plasmid was generated by inserting the hGFAP_{MIN} promoter from pAAV-GFAP-EGFP (a gift from Bryan Roth, Addgene # 50473) into pCAG-PBase plasmid (a gift from Paolo Salomoni).⁷³ hGFAP_{MIN}-SpCas9-T2A-PBase plasmid was generated by introduction of SpCas9-T2A into hGFAP_{MIN}-PBase.

PiggyBac plasmids

'EF1a-tdTomato' was a gift from Paolo Salomoni.⁷³ For the Nf1 model, hGFAP_{MIN} and iCRE sequences were inserted from hGFAP_{MIN}-PBase and pBOB-CAG-iCRE-SD (a gift from Inder Verma, Addgene # 12336) into EF1a-tdTomato PB vector. sgRNAs targeting Nf1 and Pten were cloned upstream of the EF1a-tdTomato sequence, as described above. For the Pdgfr model, hGFAP_{MIN}-iCRE sequence from Nf1 PB vector above was cloned into EF1a-TdTomato-CAG-Pdgfr (D842V) (a gift from Paolo Salomoni).⁷³ For the EGFR model, EGFRvIII was PCR-amplified and cloned into the Pdgfr PB vector to replace PdgfraD842V. To generate the EGFR-H2B-GFP PiggyBac plasmid, the EGFR model PB plasmid was modified as follows. hGFAP_{MIN}-iCRE sequence was replaced with a U6-sgRNA sequence targeting *Cdkn2a*, as described above. To introduce the H2B-GFP reporter, the tetracycline inducible expression construct was PCR-amplified from pCW57.1 (a gift from David Root, Addgene # 41393) and the H2B-GFP reporter was PCR-amplified from LV-GFP (a gift from Elaine Fuchs, Addgene # 25999)⁸⁶ and cloned after the tdTomato sequence as a

polycistronic construct with a T2A linker. For organotypic regional implantation studies Ef1-a-tdTomato of the Nf1 PB plasmid was replaced by PGK-mtagBFP2 (synthesized by Azenta life sciences).

Flow cytometry analysis

Brains were collected into ice-cold HBSS media and dissected into 1mm coronal sections using a brain matrix as above (WPI, RBMS-200C). The following regions were isolated under fluorescence guidance: tumor bulk, tumor margin and an equivalent area from the contralateral side (unless otherwise specified). Tissue was mechanically dissociated into small pieces, followed by enzymatic dissociation using Liberase TL (Roche, 0540119001) supplemented with DNase I (Sigma, 101041590001) for 30 min at 37°C; Following addition of EDTA to stop the enzymatic reaction, cells were washed with PBS and filtered through a 70 μ m cell strainer (Falcon, 352350) to remove large debris. After a blocking step in serum and Fc receptor blocking cocktail containing fetal bovine, mouse, rabbit and rat serums and anti-CD16/32 antibody (BioXCell, BE0307) for 20 min on ice, cell suspensions were incubated with antibodies and fixable viability dye eFluor780 (eBioscience, 65-0865-18, 1:1000) at 4°C for 20 min. For detection of intracellular epitopes, cells were fixed and permeabilized using BD CytoFix/CytoPerm kit (BD, 554714) for 20 min at 4°C in the dark for all panels except for the immune population panel and for analysis of iNPC markers in CD1 nude mice/littermates which were fixed/permeabilized for 2 h at 4°C in the dark (Foxp3 Transcription Factor Staining Buffer Set, eBioscience, 00-5523-00). All centrifugation steps were carried out at 820g for 2 min and 820g for 5 min following permeabilization. Samples were acquired on a BD FACSymphony flow cytometer. Myelin removal was carried out prior to staining (Miltenyi Biotech, 130-096-731) for analysis of iNPC markers in CD1 nude mice/littermates.

the following antibodies were used: rat anti-CD45-BUV563 (1:300, Clone 30-F11, BD, 612924), rat anti-CD11b-BUV661 (1:400, Clone M1/70, BD, 565080), mouse anti- β 2-microglobulin-BUV805 (1:100, Clone S19.8, BD, 749215), mouse anti-MHC Class I H-2K^b-BV510 (1:400, Clone AF6-88.5, Biolegend, 116523), rat anti-Bst2 (CD317)-BV650 (1:200, Clone 927, BD, 747605), rat anti-MHC Class II (I-A/I-E)-BV711 (1:800, Clone M5/114.15.2, BD, 563414), rabbit anti-RFP (1:100, Antibodies Online, ABIN129578) with donkey anti-rabbit AF594: rat anti-CD74-BUV395 (1:200, Clone In-1, BD, 740274), rat anti-Ki67-eFluor450 (1:400, Clone SolA15, eBio, 48-5698-80), rat anti-Bst2-BV650 (1:200, Clone 927, Biolegend, 127019), rat anti-CD44-BV786 (Clone IM7, Biolegend, 103059), rat anti-GFP-AF488 (Clone FM2-64G, Biolegend, 33807), mouse anti-Nk1.1-BUV395 (1:300, Clone PK136, BD, 564144), rat anti-CD4-BUV496 (1:300, Clone GK1.5, BD, 564667), rat anti-CD3-BUV737 (1:300, Clone 17A2, BD, 564380), rat anti-CD8a-BUV805 (1:300, Clone 53-6.7, BD, 564920), rat anti-FoxP3-eFluor 450 (1:100, Clone FJK-16S, eBioscience, 48-5773-82).

Data was analyzed using Flowjo (v10.7.1; RRID:SCR_008520). Data was compensated and only viable singlets were used for downstream analysis. For the analysis of tumor cells, CD45 and CD11b markers were used to exclude the hematopoietic compartment. Non-hematopoietic cells were gated based on tdTomato expression and a minimum of 1,500 cells (tdTomato⁺ cells for bulk and margin regions, and tdTomato⁻ for contralateral region) were used for further analysis. UMAP visualization of GFP, CD44 and BST2 markers was performed on concatenated data from 5 tumors.⁸⁷ Positive populations were manually gated based on fluorescence minus one controls (FMO) and projected onto UMAP to compare marker distribution between GFP⁺ and GFP⁻ populations.

To study the immune cell infiltration, CD45 and CD11b were used to identify the hematopoietic compartment. Main immune populations were manually gated as follows: Macrophages (CD45^{high} CD11b⁺), Microglia (CD45^{low} CD11b⁺), CD8 T cells (CD45⁺ CD11b⁻ CD3⁺ NK1.1⁻ CD8⁺), CD4 T cells (CD45⁺ CD11b⁻ CD3⁺ NK1.1⁻ CD4⁺), CD4 Teff (CD45⁺ CD11b⁻ CD3⁺ NK1.1⁻ CD4⁺ FoxP3⁺), CD4 Tregs (CD45⁺ CD11b⁻ CD3⁺ NK1.1⁻ CD4⁺ FoxP3⁺), Natural killers (CD45⁺ CD3⁺ NK1.1⁺), Natural killer T cells (NKT) (CD45⁺ CD3⁺ NK1.1⁺).

Fluorescence-activated cell sorting for collection of single cells for RNA-sequencing

For scRNA-seq, brains containing tumors were collected and dissected into 1mm coronal sections using a brain matrix (WPI, RBMS-200C). The tumor bulk and invasive tumor front migrating into the striatum (margin) were micro dissected from the sections under fluorescence guidance. The margin was defined based on tdTomato fluorescence intensity and the region extending approximately 1–2 mm away from the bulk was micro-dissected (see Figure S5B). Brain regions were enzymatically dissociated to single cells using papain dissociation, as described above. Cells were resuspended into FACS buffer supplemented with RNase inhibitors (2.5 mM HEPES, 1 mM EDTA, 1.5% BSA, 2.5% RNase) and DAPI was added 5 min prior sorting (1:10,000; Insight Biotechnology, sc-3598).

Fluorescence-activated cell sorting was performed on a BD FACSAria Fusion Class II Type A2 Biosafety Cabinet. Control tissue was processed in parallel to determine gating for the tdTomato⁺ tumor cells.

For Smart-seq2, cells were sorted into 96 well plates containing RNA lysis buffer (0.2% Triton-100, 1U/ μ l RNase inhibitor Takara Bio, 2313A). For quality control purposes, half of each plate was sorted with tumor cells from the margin and the other half with tumor cells from the bulk, leaving one empty well. After sorting, plates were snap frozen on dry ice and then stored briefly at –80°C until library preparation. For 10x scRNAseq cells were collected into 0.04% BSA in PBS and libraries prepared immediately as described below.

Single cell RNA library preparation (Smart-seq2)

Full-length single-cell RNA-seq libraries were prepared using the Smart-seq2 protocol with minor modifications.³⁵ Briefly, freshly harvested single cells were sorted into 96-well plates containing the lysis buffer (0.2% Triton-100, 1U/ μ l RNase inhibitor Takara Bio, 2313A). Reverse transcription was performed using SuperScript II (ThermoFisher Scientific, 18064014) in the presence of 1 μ M oligo-dT30VN (IDT), 1 μ M template-switching oligonucleotides (QIAGEN), and 1M betaine (Sigma 61962). cDNA was amplified using

the KAPA HiFi Hotstart ReadyMix (Kapa Biosystems KK2601) and IS PCR primer (IDT), with 24 cycles of amplification. Following purification with Agencourt Ampure XP beads (Beckmann Coulter A63881), product size distribution and quantity were assessed on a Bioanalyzer using a High Sensitivity DNA Kit (Agilent Technologies 5067–4628). A total of 140pg of the amplified cDNA was fragmented using Nextera XT DNA sample preparation kit (Illumina FC-131-1096) and amplified with Nextera XT indexes (Illumina FC-131-1001). Products of each well of the 96-well plate were pooled and purified twice with Agencourt Ampure XP beads. Final libraries were quantified and checked for fragment size distribution using a Bioanalyzer High Sensitivity DNA Kit. Pooled sequencing of Nextera libraries was carried out using a HiSeq2500 (Illumina) to an average sequencing depth of 0.5 million reads per cell. Sequencing was carried out as paired-end (PE75) reads with library indexes corresponding to cell barcodes.

Single cell RNA library preparation (10x)

Library preparation was carried out as per the 10x Genomics Chromium single-cell protocol using the v3.1 dual-index chemistry reagent kit. Suspended cells were loaded onto individual channels of a Chromium Single-Cell Chip with the reverse transcription master mix and single cell 3' gel beads. A two-step cDNA purification process was used with Dynabeads, followed by SPRISelect beads (Beckman Coulter). Samples were quantified using Qubit and normalized to achieve the desired median read depth per cell (target mean 60,000 reads per cell). Libraries were sequenced on an Illumina 2500 in High Output mode using the 10x Genomics recommended sequencing parameters.

Single cell RNA-seq data analysis (Smart-seq2)

Data pre-processing

After sequencing, libraries were inspected with the FastQC suite to assess the quality of the reads. Reads were then demultiplexed according to the cell barcodes and mapped on the mouse reference genome (Gencode release 21, GRCm38 (mm10)) with the RNA pipeline of the GEMTools 1.7.0 suite using default parameters (6% of mismatches, minimum of 80% matched bases, and minimum quality threshold of >26).⁸⁸ For all samples, cells with <65% of mapped reads or <100,000 of total mapped reads were discarded. Cells in the 95% percentile of the distribution of detected genes were included in the downstream analysis, resulting in read count matrices containing 957 (EGFR), 1033 (Pdgfr) and 834 (Nf1) cells. Genes that were expressed in fewer than five cells were removed.

Clustering

Filtering, normalization, selection of highly variable genes (HVG), clustering and genotype integration of cells were performed according to the Seurat package (version 2.3.4).⁷⁵ Through this pipeline, read counts were log-normalized for each cell using the natural logarithm of 1+ counts per ten thousand. To avoid spurious correlations, genes were scaled and centered after library sizes were regressed out. These scaled z-scores values are then used as normalized gene measurement input for the clustering and to visualize differences in expression between cell clusters. Selection of HVG was based on the evaluation of the relationship between gene dispersion and the log mean expression (with default parameters), while their total number was limited to 3,000 genes, which was close to the average of genes per cell in EGFR and Nf1 models, while Pdgfr cells displayed around 5,000 genes.

The clustering procedure projects HVG onto a reduced dimensional space before grouping cells into subpopulations by computing shared-nearest-neighbors (SNN) based on Euclidean distance. The clustering algorithm is a variant of the Louvain method, which uses a resolution parameter to determine the number of clusters.⁸⁹ The resolution parameter was set depending on both the observed heterogeneity and the biological interpretation of the resulting clusters. At this step, the dimension of the subspace was represented by the number of significant principal components (PC), which was decided based on the distribution of the PC standard deviations and by the inspection of the ElbowPlot graph. Cluster identities were assigned using previously described genes and cluster-specific markers obtained by differential expression analysis. UMAPs were used to visualize clusters and gene expression of biological relevant markers and signatures.

Data integration

After the three GBM models were analyzed and annotated independently, they were integrated to find common patterns. The integration was performed by using the Seurat package, by which allows identification of biological corresponding cells (anchors) between pairs of datasets, allowing data harmonization and comparison across tumors of different genotype. The algorithm makes use of the Canonical Correlation Analysis (CCA), a method that is able to learn gene correlation structures which are conserved across datasets.⁹⁰ To do that, it identifies a fixed number of genes (i.e. the anchor feature parameter; in this case we used 6,000 genes) that are then used to find relationships between cells across the different datasets.

Differential expression and GO analysis

Cluster-specific markers were identified through the Seurat function FindAllMarkers using the Wilcoxon's rank-sum test. The top 100 positive markers of each cell type were used as the signature for that type in order to compare them with external signatures. To visualize the similarity between cell type annotations from other studies, we applied matchScore2,⁹¹ which computes Jaccard Index to quantify the overlap between cell-type signatures. Gene Ontology enrichment analysis was performed with the simpleGO package.

Single-cell RNA-seq (10x) data pre-processing and analysis

A FASTA and GTF file of mm10 was modified to contain eGFP, tdTomato and EGFR sequences (complete with associated UTRs), raw reads were then mapped to this reference using cellranger count (v5.0.1). Expression matrices were analyzed using the Seurat package (v4.0.3, Stuart et al. 2019). Cells with mitochondrial reads making up >10% total read content, or with less than 400 genes detected, were removed. Final cell counts after filtering were 16,230. Reads were then normalized using the NormalizeData function. Gene signature scores were calculated by summing the scaled values of the genes in each signature.

Analysis of publicly available human datasets

Gene signatures for mouse Astro pr-like, Astro-like and iNPC-like states were calculated using AUCell based on the top 30 cell type marker genes. The top 500 marker genes up regulated in cells from peritumoral/tumoral area relative to core cells across patients from the Yu et al. dataset were identified using Wilcoxon signed-rank test and the intersection between these genes and mouse cell type marker genes used as input for gene enrichment analysis (R package fgsea). The mean of normalized enrichment scores (NES) across patients was calculated and shown. For survival analyses, patients were assigned to enriched/not-enriched groups based on expression levels of relevant genes, where above 90% and below 10% quantile was considered enriched and not enriched, respectively (R package survfit). The following datasets were used: the Ivy dataset downloaded from <https://glioblastoma.alleninstitute.org/static/download.html>; the Chinese Glioma Genome Atlas (CGGA) downloaded from <http://www.cgga.org.cn/download.jsp> and The Cancer Genome Atlas (TCGA) GBM dataset downloaded via R package TCGAbiolinks.

Digital pathology

Cell detection and validation

We applied supervised and semi-supervised algorithms to identify the exact location of T cells and H2B-GFP⁺ LRC in immunofluorescence confocal tile scan images. From each image, we extracted the channels of GFP (H2B-GFP LRC), AF647 (T cells), and DAPI. All image processing was carried out using QuPath⁷⁶ and ImageJ⁷⁴ software. For T cells, we ran a cell segmentation and trained a supervised Random Trees classifier with 1140 annotations for training and 742 annotations for validation from non-overlapping regions. To detect GFP tumor cells, we implemented a Random Trees classifier with a semi-supervised pipeline, allowing for an increase the detectability while maintaining the original label intensity of tumor cells. For the semi-supervised algorithm, we first trained a Random Trees classifier (classifier gfp v.1) with 1,000 annotations on GFP cancer cells and 1,000 annotations for the background. As the classifier gfp v.1 includes the bias of the observer, it is not able to detect low-intensity GFP cells; then on the same tile, we increased the brightness and contrast (automatic B&C ImageJ). We applied the classifier gfp v.1 on that image and saved the predictions that served as new annotations for the original GFP (non-auto B&C) allowing us to train a new classifier (classifier gfp v.2). That approach maximizes the detection of cells with lower intensities (fast-cycling cells). To validate the classifier gfp v.2, 860 independent annotations were made in non-overlapping regions with the training annotations. To compute the balanced accuracy of the T and GFP cell classifiers, we obtained a binary mask for the predicted cells by each algorithm. We quantified true positive, true negative, false positive or false negative frequencies according to the value of the binary mask for the annotations' coordinates (caret R package).⁷⁷ Finally, we run a simple cell segmentation on the DAPI channel and obtained a dilated binary mask to remove detected GFP cells without DAPI.

This detection method allowed us to obtain the location of each cell within the sample. Only for GFP tumor cells, we saved features related to intensity as a surrogate of the proliferative status at single-cell resolution to assess spatial relationships of dormant and proliferative tumor cells with immune cells. Due to the similarity between CD4 and CD8 markers, we use the same algorithm for immune cells detection. All the images were formatted to 8-bit with intensity values ranging from 0 to 255.

Spatial metrics for co-localization of T cells and H2B-GFP LRC

LRC and proliferative phenotypes were identified by applying unsupervised k-means clustering with $k = 3$ on the single-cell maximum intensity value. This identified GFP cell with low, medium and high intensity. The clustering was applied independently to each sample. This allowed us to examine the spatial relationship between T cells and GFP^{high} and GFP^{low} cells through a distance-based approach and an abundance-based approach.⁹²

The distance-based approach consists of representing the distribution of H2B-GFP⁺ cells (GFP^{high} and GFP^{low}) and T cells in each sample as a network, where cells are the node and the distance between neighboring cells are the links. For each sample, we run a Delaunay triangulation algorithm allowing us to obtain the spatial network and the distance between cells. We evaluated if the distance between cells differed between the two classes of links that connect (1) T cells and GFP^{low} cells and (2) T cells and GFP^{high} cells. As a second explanatory variable, we compared the distance between (1) CD4⁺ and GFP cells and (2) CD8⁺ and GFP cells, grouping GFP^{low} and GFP^{high} cells. With these two explanatory variables, link class and T cells, we built a linear mixed model (lme4 R package),⁷⁸ with the logarithm (log10) of the distance as the response variable, link class and T cells as fixed factors, link class nested in T cells, and the sample as an explanatory variable with a random effect. If the null hypothesis for the fixed factor is rejected, we evaluate *a posteriori* comparisons between the corresponding factor levels applying single-step p value adjustment for multiple comparisons.

For the abundance-based approach we computed a discrete colocalization measure based on the application of Morisita's dispersion and Morisita-Horn overlap indices⁴ on the local co-occurrence of CD4 T cells and GFP^{low} or GFP^{high} cells. For each sample, we

computed the Morisita dispersion index (Equation 1) at different spatial scales defined by the number of square quadrants or patches implemented by the R package IDmining,⁹³ that measures the degree of randomness in cell distribution.

$$I_{\delta} = Q \frac{\sum_{i=1}^Q n_i(n_i - 1)}{N(N - 1)} \quad (\text{Equation 1})$$

The algorithm subdivides the region of interests in Q quadrants or patches with a value of the diagonal (δ) and computes I_{δ} based on the abundance of cells (n_i) in the patch and the total number of cells or points (N). We iterated the algorithm from one to 90K subdivisions (patches) for each sample and took the value of the diagonal that maximizes I_{δ} , as the distance where the spatial pattern diverges the most from complete spatial randomness. The value, which is sample-dependent, was used to create a polygonal grid for each sample and compute the Morisita-Horn overlap index (Equation 2) that calculates the probability to detect two classes of cells, for simplicity x and y , in the same quadrant with a similar relative abundance

$$MH = 2 \frac{\sum_{i=1}^Q x_i y_i}{XY \left(\frac{\sum_{i=1}^Q x_i^2}{X^2} + \frac{\sum_{i=1}^Q y_i^2}{Y^2} \right)} \quad (\text{Equation 2})$$

Where x_i and y_i are the quadrant abundances of the classes and X and Y are the sample abundance of the classes. We computed the MH index at two scales within T cell hotspots identified computing Getis-Ord G^* and outside these hotspots. We tested with a one-sided t-student if the observed MH $\text{GFP}^{\text{high}}\text{-CD4}$ or $\text{GFP}^{\text{high}}\text{-CD8}$ differs from 0 (null hypothesis is that the observed colocalization matches the expected for a random distribution). Additionally, with a general linear model (GLM), we tested if the MH GFP^{high} differs between T cell types, adding the T cells/GFP ratio as a covariate. The statistical evaluation was made independently at both scales (inside and outside of immune hotspots). The normality of the variables, raw and residuals, was confirmed with a Shapiro-Wilk normality test.

Assessment of colocalization between T cells and GFP subpopulations

Within samples, the abundance of GFP^{low} and GFP^{high} cells is expected to differ because a relative minority of tumor cells remains low-cycling (GFP^{high}). To compute comparable MH indices between T cells and GFP subpopulations (low and high) we therefore controlled for differences in abundance to rule out density biases. After patch detection with the Morisita dispersion index (Equation 1), we computed the Morisita-Horn overlap index for randomly sampled GFP^{low} cells where their abundance equals the observed abundance of GFP^{high} . For each sample, random sampling was run 500 times; hence obtaining 500 values of MH between GFP^{low} and the corresponding T cell class. We compute a z-test to evaluate if the observed MH $\text{GFP}^{\text{high}}\text{-T}$ cell is higher than the mean MH $\text{GFP}^{\text{low}}\text{-T}$ cell index from the random resampling for each sample.

QUANTIFICATION AND STATISTICAL ANALYSIS

All statistical analyses were performed using Prism (GraphPad, RRID:SCR_002798). Statistical details of experiments can be found in the figure legends. Significance is stated as follows: $p > 0.05$ (ns), $p < 0.05$ (*), $p < 0.01$ (**), $p < 0.001$ (***), $p < 0.0001$ (****).